

Improving PSF modelling for weak gravitational lensing using new methods in model selection

Barnaby Rowe*

Institut d'Astrophysique de Paris, UMR7095 CNRS, Université Pierre et Marie Curie – Paris 6, 98 bis, Boulevard Arago, 75014 Paris, France

26 October 2018

ABSTRACT

A simple theoretical framework for the description and interpretation of spatially correlated modelling residuals is presented, and the resulting tools are found to provide a useful aid to model selection in the context of weak gravitational lensing. The description is focused upon the specific problem of modelling the spatial variation of a telescope point spread function (PSF) across the instrument field of view, a crucial stage in lensing data analysis, but the technique may be used to rank competing models wherever data are described empirically. As such it may, with further development, provide useful extra information when used in combination with existing model selection techniques such as the Akaike and Bayesian Information Criteria, or the Bayesian evidence. Two independent diagnostic correlation functions are described and the interpretation of these functions demonstrated using a simulated PSF anisotropy field. The efficacy of these diagnostic functions as an aid to the correct choice of empirical model is then demonstrated by analyzing results for a suite of Monte Carlo simulations of random PSF fields with varying degrees of spatial structure, and it is shown how the diagnostic functions can be related to requirements for precision cosmic shear measurement. The limitations of the technique, and opportunities for improvements and applications to fields other than weak gravitational lensing, are discussed.

Key words: gravitational lensing – methods: data analysis – methods: statistical – cosmology: observations – cosmology: large-scale structure of the Universe.

1 INTRODUCTION

The study of weak gravitational lensing (see, e.g., Schneider 2006 for a recent review) promises much as a means of detecting and measuring massive structure on cosmological scales. Through its sensitivity to all lensing mass whether baryonic or exotic, weak lensing potentially provides direct measurement of the cosmological matter power spectrum (e.g. Fu et al. 2008), a means of relating this power to visible structure (e.g. Hoekstra et al. 2005; Mandelbaum et al. 2006; Tian, Hoekstra & Zhao 2009), and the mapping of individual clusters and super-clusters (e.g., Massey et al. 2007a; Hoekstra 2007; Heymans et al. 2008). However, extracting an unbiased and uncontaminated shear signal from real telescope images in current and upcoming surveys represents an unprecedented technical challenge.

Much work has gone into testing and refining the many competing weak lensing data processing pipelines, using simulations of survey imaging data with known input lensing signals (Heymans et al. 2006; Massey et al. 2007b; Bridle et al. 2008). This simulation work has understandably concentrated upon the problem of shear measurement from noisy galaxy images, after their convolution with an anisotropic telescope point spread

function (PSF) and subsequent pixelization onto CCD arrays. However, there are other important stages in any weak lensing analysis that have been subjected to less scrutiny, such as: stacking and dithering of exposures to create science images, selection of stars for PSF modelling, colour dependence of instrument PSFs when using broad band filters, and the accurate modelling of the spatial variation of the PSF across the telescope field of view. Paulin-Henriksson et al. (2008) and Paulin-Henriksson, Refregier & Amara (2009) have recently conducted work into the amount of information required for characterizing typical PSFs at a given point, described in terms of ‘complexity’ and ‘sparsity’, but the amount of information about the overall spatial variation across the sky is less well-addressed by the literature. Moreover, this spatial variation in the PSF is purposefully ignored by current shear measurement testing simulations (e.g., Bridle et al. 2008), reserved as a separate issue.

The work in this paper is motivated towards finding ways to improve this aspect of PSF modelling, which traditionally takes the form of fitting polynomial surfaces to quantities that represent important properties of the PSF. In the KSB method (Kaiser, Squires & Broadhurst 1995; Hoekstra et al. 1998) these quantities are frequently the two components of stellar anisotropy correction, estimated using the measured ellipticities of stars in the field of view. For techniques that model PSFs with shapelet ba-

* E-mail: rowe@iap.fr

sis functions (see, e.g., Bernstein & Jarvis 2002; Refregier 2003; Refregier & Bacon 2003; Massey & Refregier 2005) it is the spatial variation in each shapelet coefficient that is described using parametrized surfaces. Regardless of the quantity being modelled there is considerable freedom in the choice of the functional form of the fitting surface (see, however, Rhodes et al. 2007; Jarvis, Schechter & Jain 2008 for physically motivated PSF models), and simple bivariate polynomials are typically used. Known problems with polynomial fitting surfaces, including reduced stability at field edges and corners, have been noted but not necessarily tackled beyond suggestions of other, perhaps better behaved, functional schemes (e.g., Van Waerbeke, Mellier & Hoekstra 2005, who used dense stellar fields to characterize structure in the PSF). Choices must also be made as to whether to model the PSF independently in areas imaged by different CCD chips, and how to weight stars of different signal to noise in the same fit. Unfortunately there is often little guidance from the data itself, as accurately estimating the uncertainty on a stellar ellipticity measurement or shapelet coefficient is difficult.

One recent development has been the suggestion of Principal Component Analysis (PCA) as a means of building up knowledge of the PSF (Jarvis & Jain 2004; Schrabback et al. 2009), allowing the use of more complex polynomial surfaces coupled with a more rigorous quantification of the degree of information redundancy. The technique uses a large number of images to explore the principle vectors in the space of observed PSF models, and will clearly form a crucial part of future PSF modelling for large surveys. Using PCA, overfitting can be controlled whilst ensuring that all the observable features in the PSF are properly modelled. However, this approach has one important caveat: it assumes that there is no independent random or complex quasi-random component to the PSF anisotropy in any given field. This assumption will conceivably be broken for ground-based data (possibly even from space), specifically if the anisotropy is a combination of predictable *and* complex or chaotic effects. In this paper the investigation will instead focus upon a complementary question: whether there are further tests of the modelling quality of a single PSF anisotropy map, including those created using PCA, without requiring it be drawn from a physically predictable underlying distribution.

Tests for overall control of systematics, and indirectly therefore the quality of the PSF model, do exist in weak lensing once the shear signal can be decomposed into E-mode/B-mode components (e.g., Crittenden et al. 2002; Schneider et al. 2002). However, these tests are only possible *after* the lensing shear is measured, at the end of the analysis, and B-modes may also be generated by intrinsic alignments and source clustering. An important investigation into the effects of imperfect PSF modelling was performed by Hoekstra (2004), who analyzed residual correlations in PSF models using the aperture-mass statistic and studied the impact of these correlations upon cosmic shear measurements. This paper naturally follows on from that work by providing a formal discussion of the reasons for residual correlations in poorly modelled data. In addition, it presents a first investigation into whether such correlations may be used as an aid to the systematic selection of PSF modelling schemes, and as an aid to modelling in general.

The assessment of goodness of fit (see, e.g., Lupton 1993) of a given model to the physical data is a vital stage in any scientific analysis, and the related field of model selection is attracting increasing interest within astronomy as a means of evaluating evidence for competing cosmological models (for recent reviews in astrophysical contexts see Liddle, Mukherjee & Parkinson 2006 and Trotta 2008; for recent discussions and applications see, e.g.,

Liddle 2007; Efstathiou 2008; Kurek & Szydlowski 2008). Estimates and uncertainties upon model parameters derived from any fit are meaningless if the model itself is an unlikely match to the data, and if further analyses depend upon the accuracy or stability of this model then later conclusions may be biased or subject to unnecessary additional variance (Paulin-Henriksson et al. 2009). The problem can become acute in applications where empirical or unverified physical models must be used, or where errors upon measured data points are difficult to estimate accurately. These problems are precisely those encountered when attempting to model the spatial variation of the PSF in weak lensing applications.

The most famous and often-used diagnostic of goodness of fit is the chi-squared statistic (see Lupton 1993), and simple chi-squared per degree of freedom arguments are often used as a means of model selection (see, e.g., Spergel et al. 2007). A related measure that generalizes to non-Gaussian distributions is the Akaike Information Criterion (AIC), derived from an approximate minimization of the Kullback-Leibler information entropy (see, e.g., Liddle et al. 2006; Trotta 2008). Bayesian probability theory (see Gelman et al. 2003 for a comprehensive general reference) also provides two further guides to model selection: the full calculation of the Bayesian evidence, and its related approximation the Bayesian Information Criterion (BIC: again see Trotta 2008). These criteria all use calculations of the statistical likelihood \mathcal{L} of a dataset given the model in question, either the via integration of \mathcal{L} over the full possible parameter space in the case of the Bayesian evidence, or by comparison of the best-fitting model maximum likelihood \mathcal{L}_{\max} to the number of parameters in the model. In order to reliably calculate these ‘data-given-model’ likelihoods, the probability distributions $p(y_i)$ of individual measured data points y_i must be known or well-approximated; as discussed above, this is seldom the case in PSF modelling contexts.

One important topic of this paper is to discuss other properties of the relationship between model and data that can be usefully explored without good prior knowledge of the uncertainties upon individual data points. A related investigation, merely initiated by this work, will be to begin to understand what information is being lost when employing model selection arguments based entirely upon data-given-model likelihoods or related criteria. As will be shown, such information may be of use when diagnosing goodness of fit. The spatial correlation of residuals for both underfitting and overfitting models is partly predictable, and this insight can also be used to guide modelling improvements in a way that conforms to the principle of Occam’s Razor.

The structure of this paper is as follows: in Section 2 a basic theory of correlations in model residuals is described, specifically aimed at models of stellar ellipticity. This leads to the construction of two independent diagnostic functions, and makes predictions for the behaviour of these functions for under- and overfitting models. Section 3 then applies these diagnostics to a test-case scenario of a simulated starfield with a known underlying PSF anisotropy model. In Sections 4 & 5 these tests are repeated on a suite of simulated starfields with varying degrees of spatial structure in the PSF map. Relating the diagnostics to requirements for cosmic shear surveys is discussed in Section 6. In Section 7 the possibility of a generalized extension beyond weak lensing is discussed, followed in Section 8 by a general summary and conclusions.

2 SPATIAL CORRELATIONS IN MODEL RESIDUALS

2.1 Basic theory and assumptions

The starting point in this analysis is to construct a simplified description of the process of modelling PSF anisotropy across the x - y plane, such as across a telescope field of view. In what follows the discussion is limited to models of complex, spin-2 pseudo-vector fields (i.e. $f(x, y) = |f|(x, y)e^{i2\theta(x, y)}$) on a 2D plane, but such arguments may be generalized to scalar or spin- n fields, and to other spatial dimensionalities (see Section 8).

An observed complex ellipticity field is described as the sum of two contributions, the unknown ‘true’ ellipticity field e_t and N , a stochastic complex variable describing noise upon ellipticity measurements. This field is labelled $e(x, y) = e_1 + ie_2$, where:

$$e = e_t + N. \quad (1)$$

In almost all that follows the explicit x - y dependence of fields such as e_t will be dropped for brevity, and should be implied. The description of discrete observations e_i by a continuous ‘quasi-field’ e is also a notational convenience: measured quantities will always be an $e(x_i, y_i)$ sample of the proposed field e . We assume that the stochastic noise term satisfies $\langle N \rangle = 0$.

If a best fit parametrized model is then applied to describe e , one can choose to write the modelled ellipticity e_m as

$$e_m = e_t + m(e_t, N; f_m), \quad (2)$$

where $m = e - e_t$ will hereafter be referred to as the *inaccuracy* in the model, also unknown, and f_m is simply a label denoting the functional scheme used to fit the spatial variation of e (e.g. a second order bivariate polynomial). This expression makes explicit the dependence of the inaccuracy m upon e_t , the ensemble of discrete realizations of N , and f_m . In general this dependence will be non-trivial to describe, but the aim of this paper is to look for diagnostic tests by which the functional properties of m can be constrained.

The principal tool in this work is the two point ellipticity correlation function, the observable quantity used to extract signal in cosmic shear studies. In this the investigation follows Hoekstra (2004), as well as the later work of Van Waerbeke et al. (2005) and Hoekstra et al. (2006), in analyzing correlations in corrected PSF patterns as a means of testing anisotropy models. Specifically the $\xi_{\pm}(r)$ correlation functions will be used, defined as

$$\xi_{\pm}(r) = \langle e_{\tan}(\mathbf{x} + \mathbf{r})e_{\tan}(\mathbf{x}) \rangle \pm \langle e_{\times}(\mathbf{x} + \mathbf{r})e_{\times}(\mathbf{x}) \rangle, \quad (3)$$

where e_{\tan} and e_{\times} are the known as the *tangential* and *rotated* components of the ellipticity, and the angle brackets denote an averaging over all *pairs* of points separated by a distance r . It should be noted therefore that this definition implicitly averages over all angles, which is not a problem in the cosmic shear case where correlations are assumed isotropic so that $\xi(r) = \xi(r)$; if the field is not strictly isotropic then it must be borne in mind that $\xi(r)$ is the angular average correlation, and thus that some information may have been lost.

The tangential and rotated components are defined for the complex ellipticities e of each pair as

$$e_{\tan} + ie_{\times} = -e^{-2i\phi}(e_1 + ie_2) \quad (4)$$

(see, e.g., Schneider 2006), where ϕ is the angle between the abscissa and the line joining the location of each member of the pair

of points. With a discrete number of ellipticity measurements the quantities in equation (3) can then be estimated by

$$\xi_{\pm}(r) = \frac{1}{N_{\text{pairs}}} \sum_{\text{pairs}} e_{\tan}(\mathbf{x} + \mathbf{r})e_{\tan}(\mathbf{x}) \pm e_{\times}(\mathbf{x} + \mathbf{r})e_{\times}(\mathbf{x}) \quad (5)$$

in finite bins of r . Such correlation function estimates, when made using PSF-corrected galaxy ellipticities, are the primary observable quantity in modern studies of cosmological weak lensing (see, e.g., Fu et al. 2008; Schrabback et al. 2007).

In the following discussion, which focuses upon ξ_+ as a diagnostic of PSF modelling, frequent use will be made of a useful shorthand notation:

$$\langle e^* e \rangle \equiv \langle (e_{\tan} - ie_{\times})(e_{\tan} + ie_{\times}) \rangle \quad (6)$$

$$= \xi_+(r)$$

$$+ i \langle e_{\tan}(\mathbf{x} + \mathbf{r})e_{\times}(\mathbf{x}) - e_{\times}(\mathbf{x} + \mathbf{r})e_{\tan}(\mathbf{x}) \rangle. \quad (7)$$

Due to parity symmetry (see Schneider 2006) the imaginary second term in equation (7) tends to zero, and so $\langle e^* e \rangle(r) = \xi_+(r)$. Similarly, $\langle e_m^* e_m \rangle(r)$ will be used to denote the $\xi_+(r)$ autocorrelation in the model e_m . This notation is convenient not only as a labelling convention but also as a computational tool, and so will be used exclusively hereafter.

In order to proceed, two simplifying assumptions are made about the noise. Firstly, it is assumed that N is spatially *uncorrelated* so that

$$\langle N^* N \rangle(r) = 0 \quad (8)$$

for all $r > 0$. Secondly, it is assumed that the cross-correlation between N and the unknown e_t is also zero, so that

$$\langle e_t^* N + N^* e_t \rangle(r) = 0. \quad (9)$$

Situations in which equations (8) and (9) no longer hold can be envisaged, such as in the presence of problems with reduced Charge Transfer Efficiency (CTE) in telescope CCDs (see, e.g. Rhodes et al. 2007) or preferences for certain PSF directions due to large pixel sizes or under sampled stellar images. In this theoretical analysis these factors are assumed to be small, but if necessary the assumption may be easily tested and corrected for using simulated data.

2.2 Fit diagnostics

For an ideal fit $m = 0$ everywhere, but this is unrealistic in the case of noisy data and finite numbers of observations. For the case of an imperfect but well-constrained, stable and accurately predictive model the following three conditions should be simultaneously fulfilled:

$$\langle m^* e_t + e_t^* m \rangle(r) \simeq 0 \quad (10)$$

$$\langle m^* N + N^* m \rangle(r) \simeq 0 \quad (11)$$

$$\langle m^* m \rangle(r) \simeq 0 \quad (12)$$

for all $r > 0$. These conditions will be met if the modelling inaccuracies m can, like the noise, be approximately described as an independent, stochastic variable $m = M$ with $\langle M \rangle = 0$.

The first of these conditions (10) requires that the inaccuracies m should be distributed at random with respect to the true ellipticity distribution, and thus that the cross-correlation between these quantities be zero; this condition will be broken if the model is systematically *underfitting* the true ellipticities e_t , as will be discussed in Section 2.3 below. The second condition (11) explicitly states

that m is required to be uncorrelated with the noise N , expected if the scheme f_m allows significant *overfitting* of the data. The third and final condition (12) requires that m show no spatial autocorrelation, which will be fulfilled if the inaccuracies at all points are mutually randomly distributed. This third condition may be broken for both overfitting, where neighbouring m values may be correlated to the extent allowed by instabilities in the chosen f_m , and underfitting, where e_m systematically fails to reproduce observable features in e_t .

Unfortunately, the functions in equations (10)-(12) cannot be measured directly, as m , N and e_t are unknown. However, it is possible to construct two independent, observable correlation functions with which to attempt to constrain these quantities. There is freedom in how these are defined (as will be discussed below), but the following useful forms are suggested:

$$D_1(r) \equiv \langle (e - e_m)^* (e - e_m) \rangle (r) \quad (13)$$

$$D_2(r) \equiv \langle e^* (e - e_m) + (e - e_m)^* e \rangle (r). \quad (14)$$

These two diagnostic quantities D_1 and D_2 may be easily estimated from modelled stellar fields using routines that are standard in statistical lensing. Using the definitions and assumptions described by equations (1)-(9), they can be expressed in terms of the unknown quantities as follows:

$$D_1(r) = -\langle m^* N + N^* m \rangle (r) + \langle m^* m \rangle (r) \quad (15)$$

$$D_2(r) = -\langle m^* N + N^* m \rangle (r) - \langle m^* e_t + e_t^* m \rangle (r). \quad (16)$$

It is noted immediately that there are only two quantities with which to constrain the three unknowns of conditions (10)-(12), and the system is therefore underdetermined. This is a natural consequence of there being only two directly observable quantities (e and e_m) with which to place constraints upon correlations in m , N and e_t . The system of equations described by (15) and (16) cannot therefore be solved to demonstrate any of (10)-(12) uniquely. Instead, one may determine only a general family of solutions. In vector notation this solution is simply

$$\begin{pmatrix} \langle m^* m \rangle (r) \\ \langle m^* N + N^* m \rangle (r) \\ \langle m^* e_t + e_t^* m \rangle (r) \end{pmatrix} = \begin{pmatrix} 1 \\ 1 \\ -1 \end{pmatrix} t + \begin{pmatrix} D_1(r) \\ 0 \\ -D_2(r) \end{pmatrix} \quad (17)$$

where t is any real number. Attempts to construct a third independent observable with which to break this degeneracy do not succeed: for example, the observable function $\langle e^* e \rangle - \langle e_m^* e_m \rangle$ may be written simply as $D_2 - D_1$.

The fact that this system of equations is underdetermined means the $D_1(r)$ or $D_2(r)$ diagnostics can never be used to *prove* that $\langle m^* m \rangle = \langle m^* N + N^* m \rangle = \langle m^* e_t + e_t^* m \rangle = 0$ at all scales. However, they allow the positive diagnosis of poor modelling if either are nonzero at a significant level. Moreover, in order to be erroneously led into the belief that a given model fit is accurate and stable would require that

$$\langle m^* m \rangle \simeq \langle m^* N + N^* m \rangle \simeq -\langle m^* e_t + e_t^* m \rangle \quad (18)$$

for all scales r , constituting a significant coincidence and very poor luck. Finally, although the general expression in (17) allows an infinite family of solutions to our three quantities (10-12), this solution is not the only information we have. Further assumptions and simple reasoning may be employed so as to predict what might be expected for these diagnostic measures in the cases of over- or underfitting; this in turn may allow the tuning of modelling schemes so as to better represent the data without fitting noise. These reasoned expectations for the general form of $D_1(r)$ and $D_2(r)$ will now be outlined.

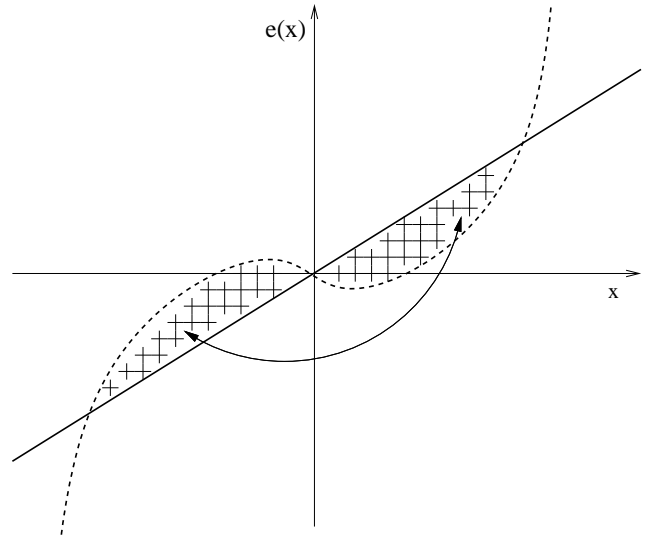


Figure 1. Schematic showing how $\langle m^* m \rangle (r)$ may be expected to be both negative and positive, depending upon scale r , for underfitting models. The dotted line is a given ‘true’ model, and the thick solid line a best-fit straight line. The model inaccuracy m will be correlated within the two cross-containing regions, but *anticorrelated* on the larger scales between the two regions, indicated by the closed arrows.

2.3 The case of underfitting

In order to describe what might be expected in the case of underfitting, we consider a hypothetical scheme f_m for which the model ellipticities e_m do not adequately represent the underlying field e_t . This can be expressed in terms of the simple model constructed in Section 2.1, and the further assumption that in the limit of *severe* underfitting it may be approximated that

$$m = m(N, e_t; f_m) \simeq m(e_t; f_m). \quad (19)$$

The validity of this approximation will depend strongly upon the degree to which a given fit fails to reproduce observable features in e_t , but it can be motivated by an illustrative example: a flat model scheme f_m for which $e_m = \langle e \rangle = \text{constant}$ being used to describe an e_t which varies significantly with x and y . In this case $m = \langle e \rangle - e_t$, which is a clear function of e_t and only very weakly dependent upon the noise via $\langle e \rangle$.

Given the assumption of equation (19), it should be expected that m is approximately uncorrelated with the noise N for underfitting models (carrying only a weak dependence upon it), and thus that

$$\langle m^* N + N^* m \rangle (r) \simeq \langle m^* (e_t; f_m) N + N^* m (e_t; f_m) \rangle \quad (20)$$

$$\simeq 0. \quad (21)$$

The condition expressed in equation (11) is therefore approximately fulfilled for underfitting models, meaning that observations of $D_1(r)$ and $D_2(r)$ will provide constraints upon the quantities in equations (10) and (12). Using equations (13) and (14), this then gives

$$D_1(r) \simeq \langle m^* m \rangle (r) \quad (22)$$

$$D_2(r) \simeq -\langle m^* e_t + e_t^* m \rangle (r). \quad (23)$$

These predictions can now be used to make further conclusions as to the expected form of these functions, allowing the positive diagnosis of underfitting models if these expected forms are observed.

From equation (19) it is clear that the form taken by $\langle m^*m \rangle$ will be related to that of $\langle e_t^*e_t \rangle$, and if the underfitting is significant then $\langle m^*m \rangle$ is likely to be nonzero on or near the scales for which $\langle e_t^*e_t \rangle$ is nonzero. Figure 1 shows a simple example of how both correlation and anticorrelation might be expected in underfitting model residuals; in this simple example of a one-dimensional underfitting model the residuals within the cross-containing regions will be positively correlated, but *between* these regions the residuals will be negatively correlated. Turning to the simple $e_m = \langle e \rangle$ model for another illustration, using equations (22) and $\langle N \rangle \simeq 0$ it may be written that $D_1(r) \simeq \langle e_t^*e_t \rangle - |\langle e_t \rangle|^2$. Therefore, this $D_1(r)$ may potentially be both positive or negative for differing ranges r , depending upon the functional form of e_t .

This behaviour will also be expected from the second measurable quantity $D_2(r)$, which from equation (23) will also be activated by underfitting: $\langle m^*e_t + e_t^*m \rangle$ will often be nonzero for $m \simeq m(e_t; f_m)$. The function $D_2(r)$ may be rewritten by considering that $m = e_m - e_t$, giving

$$\begin{aligned} D_2(r) &\simeq -\langle m^*e_t + e_t^*m \rangle \\ &= 2\langle e_t^*e_t \rangle - \langle e_m^*e_t + e_t^*e_m \rangle. \end{aligned} \quad (24)$$

Once again, $D_2(r)$ may be expected to be either positive or negative depending upon scale r and the sign of $\langle e_t^*e_t \rangle$. However, the precise dependence of $D_2(r)$ may differ from that of $D_1(r)$ in a way that is difficult to predict without detailed knowledge of the e_t field.

2.4 The case of overfitting

The case of overfitting is now considered so as to make predictions for the behaviour of $D_1(r)$ and $D_2(r)$: if the behaviour differs from the underfitting case this will allow the two cases to be distinguished and positively identified, and allow subsequent modelling improvements to be made in a guided fashion. As mentioned in Section 1, the application of PCA to PSF modelling (Jarvis & Jain 2004) also brings control over overfitting via the removal of identified low-importance principal components. However, it may be that a hybrid of PCA and the simultaneous fitting of an independent surface is necessary to account for random changes in the PSF pattern between exposures, and so a diagnosis of possible overfitting in this extra surface will still be desirable. Moreover, the behaviour of $D_1(r)$ and $D_2(r)$ in overfitting models is an interesting investigation in itself, as the technique may be useful in other situations in which PCA is not directly applicable (see Section 7).

In Section 2.3 the inaccuracy m was approximated as being a function of e_t and f_m only. A similar approximation can be argued for the opposing case of severe overfitting:

$$m = m(N, e_t; f_m) \simeq m(N; f_m). \quad (25)$$

This statement can be justified by considering what is meant by an overfitting model: one which captures not only an observable physical trend, but is also unjustifiably sensitive to random noise upon measurements. Such models will not in general be biased in a way that can be related to e_t , but will prove to be unstable with respect to changes in N (this concept is also discussed in Paulin-Henriksson et al. 2009). The correlation properties of m are now largely decided by this random quantity and inherent correlations caused by the best-fitting chosen model f_m . Taking this assumption, and using equations (25) and (9), leads to

$$\langle m^*e_t + e_t^*m \rangle(r) \simeq \langle m^*(N; f_m)e_t + e_t^*m(N; f_m) \rangle \quad (26)$$

$$\simeq 0, \quad (27)$$

via the same reasoning as equation (20). This corresponds to saying that condition (10) will be fulfilled when severely overfitting data, just as in Section 2.3 it was argued that condition (11) is automatically fulfilled if data is being underfit.

Using this result, the effects of overfitting upon the forms of $D_1(r)$ and $D_2(r)$ can be predicted. From equations (13), (14), and (27) it may be written that

$$D_1(r) = \langle m^*m \rangle(r) - \langle m^*N + N^*m \rangle(r) \quad (28)$$

$$D_2(r) \simeq -\langle m^*N + N^*m \rangle(r). \quad (29)$$

It is noted immediately that the expression for $D_1(r)$ remains unsimplified: unlike $\langle m^*e_t + e_t^*m \rangle$, the $\langle m^*m \rangle$ term will not necessarily vanish for overfitting models, despite the assumption of uncorrelated noise in equation (8). As can be seen from equation (25), there remains the possibility of correlation due to the inherent properties of the functional form of the model f_m used to unstably fit the data.

It is expected that the condition (12) is *not* fulfilled when we are overfitting the data, and thus that $D_2(r)$ will be nonzero. It can furthermore be said that a *positive* cross-correlation will be expected between N and m , so that

$$\langle m^*N + N^*m \rangle > 0. \quad (30)$$

This can be justified by considering once again $m = e_m - e_t$, which combined with equation (9) then gives

$$\langle m^*N + N^*m \rangle(r) = \langle e_m^*N + N^*e_m \rangle(r) > 0. \quad (31)$$

This last inequality indeed expresses a definition of overfitting, being that the best-fitting model e_m shows some significant average correlation with the particular realization of the noise N . It is then clear from equations (29) and (31) that

$$D_2(r) = -\langle m^*N + N^*m \rangle(r) < 0, \quad (32)$$

i.e. nowhere positive and potentially significantly negative, for overfitting models. In Section 2.3 it was seen that $D_2(r)$ is expected to be positive over some range of r for severely underfitting models. Whilst the minimization of $D_2(r)$ will lead to an optimal fit in any case, this difference in behaviour between under- and overfitting offers hope of diagnosing successfully between the two cases, allowing informed improvements in modelling to be made at each stage.

Furthermore, it can be argued that in most cases the $\langle m^*m \rangle$ due to undue freedom in the model f_m will be small compared to $\langle m^*N + N^*m \rangle$; if this is so the $D_1(r)$ function may also be used to distinguish under- and overfitting. The argument relies on the following insight: an overfitting model, but one that has nevertheless been constructed by minimizing deviations from the observed data, will in all but the most pathological cases be expected to have inaccuracies $|m(N; f_m)| \leq |N_i|$ at each point (x_i, y_i) . The limiting example of this behaviour is an ‘ultimate overfit’, for which the model is simply $e_m = e$ (and thus $m = N$), with an interpolation or spline between stellar data points. Such a model takes no account of the fact that there may be noisy or imperfect measurements among the input data. Using $|m(N; f_m)| \leq |N|$ then gives

$$\langle m^*m \rangle \leq \frac{1}{2} \langle m^*N + N^*m \rangle < \langle m^*N + N^*m \rangle \quad (33)$$

which in turn implies that

$$D_1(r) = \langle m^*m \rangle(r) - \langle m^*N + N^*m \rangle(r) < 0 \quad (34)$$

in the same way as $D_2(r)$. This offers further hope of positive,

distinguishable diagnoses of both under- and overfitting, based on whether $D_1(r)$ and $D_2(r)$ are observed to be both positive and negative, or negative only, respectively.

To summarize, the functional behaviour of the $D_1(r)$ and $D_2(r)$ diagnostic functions for both over- and underfitting modelling schemes f_m has been predicted using simple assumptions about the nature of the modelling, the noise, and the data themselves. The most important, and potentially least secure, of these assumptions are the validity of the approximate functional dependencies of m , given in equations (19) and (25). In order to test these points of reasoning, and to explore the strength of each diagnostic function in a realistic modelling situation, the following Section will test the efficacy of $D_1(r)$ and $D_2(r)$ using a simulated PSF anisotropy map with a known, underlying ellipticity model.

3 TESTS ON A SIMULATED ANISOTROPY MAP

The diagnostic functions $D_1(r)$ and $D_2(r)$ have been shown to offer some promise as diagnostics of both over- and underfitting models. The discussion has, from the start, focused upon the modelling of ellipticity fields across a plane, a process very commonly undertaken in the modelling of anisotropic PSFs for weak lensing (e.g., Kaiser et al. 1995; Hoekstra et al. 1998; Leauthaud et al. 2007; Fu et al. 2008). Improving this modelling is the primary motivation of this work, and so in order to test $D_1(r)$ and $D_2(r)$ it is appropriate to simulate modelling conditions similar to those encountered in such weak lensing analyses, exploring whether some of the simple insights of 2 hold validity in such a regime. In this Section the discussion will concentrate upon a single simulated PSF anisotropy field (hereafter referred to as simply the starfield) in order to illustrate the forms of $D_1(r)$ and $D_2(r)$ in some detail, and give visual examples.

3.1 Constructing the starfield

The simulated starfield is designed to mimic measurements of ellipticity from 2500 stars across a square telescope field of view of area 1 deg². The number of stars in the field, the field shape, typical PSF anisotropy and measurement noise are loosely based upon lensing observations from the Canada-France-Hawaii Telescope Legacy Survey-Wide (CFHTLS-W, e.g. Fu et al. 2008; Hoekstra et al. 2006). An ellipticity measurement e was assigned to each star as modelled in equation (1), consisting of a true underlying model e_t and additive noise term N , each scaled so as to resemble the CFHTLS-W.

In order to construct $e_t(x, y)$ the telescope field of view is first defined upon a set of coordinates x', y' , with both x' and y' varying in the interval $[-1, 1]$. Each component of the true field e_t was then modelled by a bivariate, fifth order Chebyshev polynomial defined as

$$(e_t)_i = \sum_{j,k=0}^{j+k \leq 5} a_{ijk} T_j(x') T_k(y') \quad (35)$$

with $i = 1, 2$ denoting the real and imaginary parts of e_t respectively, and where $T_j(x)$ is the j th order Chebyshev polynomial of the first kind (see Figure 2; also Arfken & Weber 2005). From this Figure the reason for choosing these Chebyshev polynomials becomes clear: each term in equation (35) will add contributions of similar magnitude across the interval $[-1, 1]$. The value of each a_{ijk}

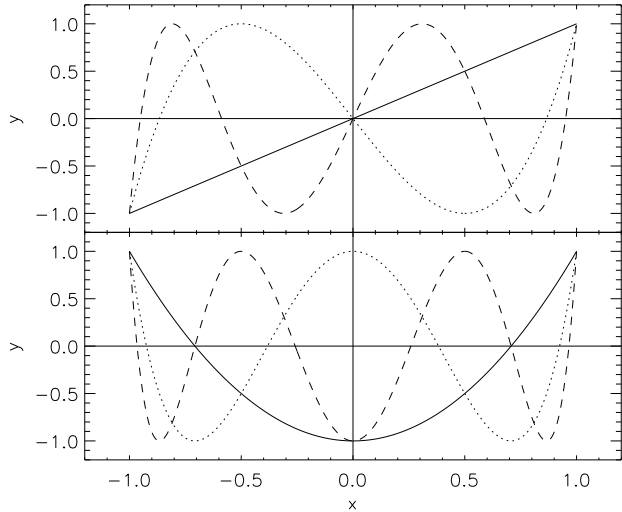


Figure 2. Lowest order Chebyshev polynomials of the first kind, plotted in the interval $x \in [-1, 1]$. Upper panel: $T_1(x)$ (solid line), $T_3(x)$ (dotted line), $T_5(x)$ (dashed line). Lower panel: $T_2(x)$ (solid line), $T_4(x)$ (dotted line), $T_6(x)$ (dashed line). The normalization properties of these functions on the chosen interval make them well-suited for simulating e_t fields with approximately equal degrees of spatial structure on varying scales.

was then assigned by random sampling from a Gaussian distribution of mean $\mu_a = 0$ and standard deviation $\sigma_a = 0.01$. The coordinates are then transformed from x', y' to an ‘observed’ x, y (in arcminutes) via

$$x' = \frac{2x}{60} - 1, \quad y' = \frac{2y}{60} - 1, \quad (36)$$

leading to a functional expression $e_t(x, y)$ across the 60×60 arcmin² simulated field of view.

The random noise N added to each component of e_t was then modelled as a Gaussian random variable with mean $\mu_N = 0$ and standard deviation $\sigma_N = 0.015$, matching scatter in ellipticity measurements for the bright stars (typically with i -band magnitude $i < 22$) used in PSF modelling in the CFHTLS-W. The resulting simulated ellipticities for this test field can be seen in Figure 3, along with the $\langle e^* e \rangle$ correlation function for the starfield.

It should be noted that whilst the amplitude and noise properties of this starfield have been designed to loosely approximate real stellar ellipticity data, no attempt has been made to ensure that the spatial variation in the underlying e_t resembles coherent physical patterns as caused by telescope focusing errors, coma or other optical phenomena (see, e.g., Jarvis et al. 2008). This is essentially a separate, although important, issue: in the following investigation the aim is merely to test whether $D_1(r)$ and $D_2(r)$ help in the correct identification of an appropriate fitting scheme f_m for the simulated starfield, i.e. whether the most successful fit is based upon a fifth order bivariate polynomial, matching the level of input spatial structure.

Nonetheless, the analysis still has practical relevance as it must be hoped that typical PSF patterns mostly fall within the space of possible starfields in the random prescription described above (otherwise polynomial fitting itself is likely to fail). In Sections 4 & 5 the testing will be extended to large sample of random starfields, precisely in order to explore the success of $D_1(r)$ and $D_2(r)$ for a variety of input ‘true’ signals. The remainder of this Section will be concerned with the success of these new diagnostics for the starfield of Figure 3.

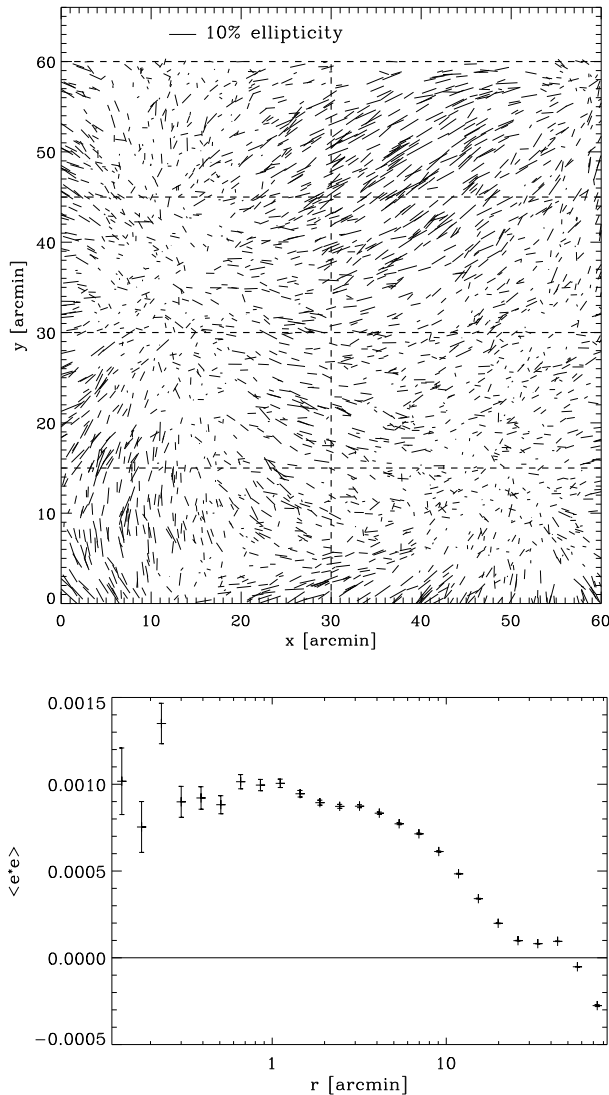


Figure 3. Upper panel (a): Whisker plot showing the positions and ellipticities of the 2500 stars in the simulated 1 deg^2 starfield, as described in Section 3.1. The simulated noise on each component of ‘measured’ ellipticity e is $\sigma_N = 0.015$. The dashed lines show the boundaries of the 8 chips defined when performing an artificial ‘chipwise’ fit to the simulated data. Lower panel (b): Autocorrelation $\langle e^*e \rangle$ in the same simulated starfield.

3.2 Fits to the starfield ellipticities

The ellipticity variation in the simulated starfield was then least-squares fit using each of a set of four different bivariate polynomial fitting schemes f_m : third, fourth, fifth (matching the input polynomial order) and sixth order simple polynomials, performing a fit to each component of ellipticity independently. The use of simple rather than Chebyshev polynomials for fitting is immaterial, as each can be formally expressed in terms of the other (at equivalent order) via exact linear transformations in the polynomial coefficients. The best-fitting model was found in each case using Singular Value Decomposition (SVD) as implemented by the IDL routine SVD-FIT.PRO, itself based upon the SVDCMP.F routine within *Numerical Recipes* (Press et al. 1992). The SVD fitting process has the property of minimizing numerical round-off error and matrix singularity problems when attempting to solve underdetermined systems of

equations, and thus even in the case of an overfitting f_m will produce the best possible solution. This is important as the diagnostic tests presented should be as insensitive as possible to numerical issues.

So as to provide a clear example of overfitting, the starfield was artificially split into eight regions associated with hypothetical CCD chips. These ‘chip regions’ can be seen in Figure 3, bordered by dashed lines. This is done to illustrate the increased potential for overfitting when modelling ‘chipwise’, as is commonly done in weak lensing (see, e.g. Fu et al. 2008, who independently model the PSF anisotropy in each of the 36 CCD chips in the 1 deg^2 CFHTLS-W field of view). However, such work only uses low-order polynomials for each chip, and it is also interesting to observe the behaviour of $D_1(r)$ and $D_2(r)$ in cases of severe (unrealistic) overfitting. Fitting chipwise we also begin to explore the question of whether modelling schemes that cannot perfectly fit e_t , i.e. a ‘wrong’ model, may be validated as practically sufficient given limited data. For this chipwise fit we adopt schemes f_m that use first, second, third and sixth order bivariate polynomial surfaces, each being fit to each chip independently.

3.3 Comparison with simple modelling diagnostics

Having fit the 2500 simulated starfield measurements of e using a set of models $e_m(\mathbf{x}; f_m)$, for a variety of different fitting schemes f_m , the diagnostic functions $D_1(r)$ and $D_2(r)$ are calculated using the formula in equation (5). Measurements are divided into 25 logarithmically-spaced angular bins between 7 arcsec and 1.4 deg. This binning scheme was chosen as fairly representing both small and large scale information. By varying these values it was also verified that $D_1(r)$ and $D_2(r)$ were stable in regards to this choice, which was found to be true once sufficient numbers of bins were used as to be able to explore small scale correlations. Uncertainties were then calculated as the standard error upon the mean value from all the pairs within each bin, therefore *not* taking the correlation in values between neighbouring bins into account. Calculations of the $D_1(r)$ and $D_2(r)$ diagnostics, for each scheme f_m , can be seen in the right hand panels of Figure 4 for the global fit and Figure 5 for the chipwise fit.

Whilst it should be noted that residual-residual correlations have already been used by some groups to rule out or justify PSF models (see, e.g., Hoekstra 2004; Van Waerbeke et al. 2005; Hoekstra et al. 2006; Schrabback et al. 2007), and that these will be compared to $D_1(r)$ and $D_2(r)$ in the following Section, the left hand panels of Figures 4 & 5 show comparative examples of more simple diagnostics used in the past to display the results of PSF model fits (see, e.g., Hoekstra et al. 1998; Heymans et al. 2005; Schrabback et al. 2007). The far left hand panels of Figures 4 & 5 show ‘whisker plots’ of $e - e_m$ (referred to as corrected ellipticities) to depict the random nature of fitting residuals. As can be seen by comparison with the corresponding $D_1(r)$ plots, correlation and anticorrelation may exist that is difficult to accurately quantify by eye, although qualitatively there are traces of correlation in the third and fourth order fit whisker plots. A correlation analysis of some sort is nonetheless clearly desirable, just as has been argued previously (Hoekstra 2004). The inner left hand panels depict the distribution of ‘original’ ellipticities e in comparison to the distribution of the corrected ellipticities $e - e_m$; once again these plots are more difficult to quantifiably interpret than $D_1(r)$ and $D_2(r)$, which show more markedly different behaviour with f_m . The question remains as to whether these new diagnostics are behaving as predicted in Section 2.

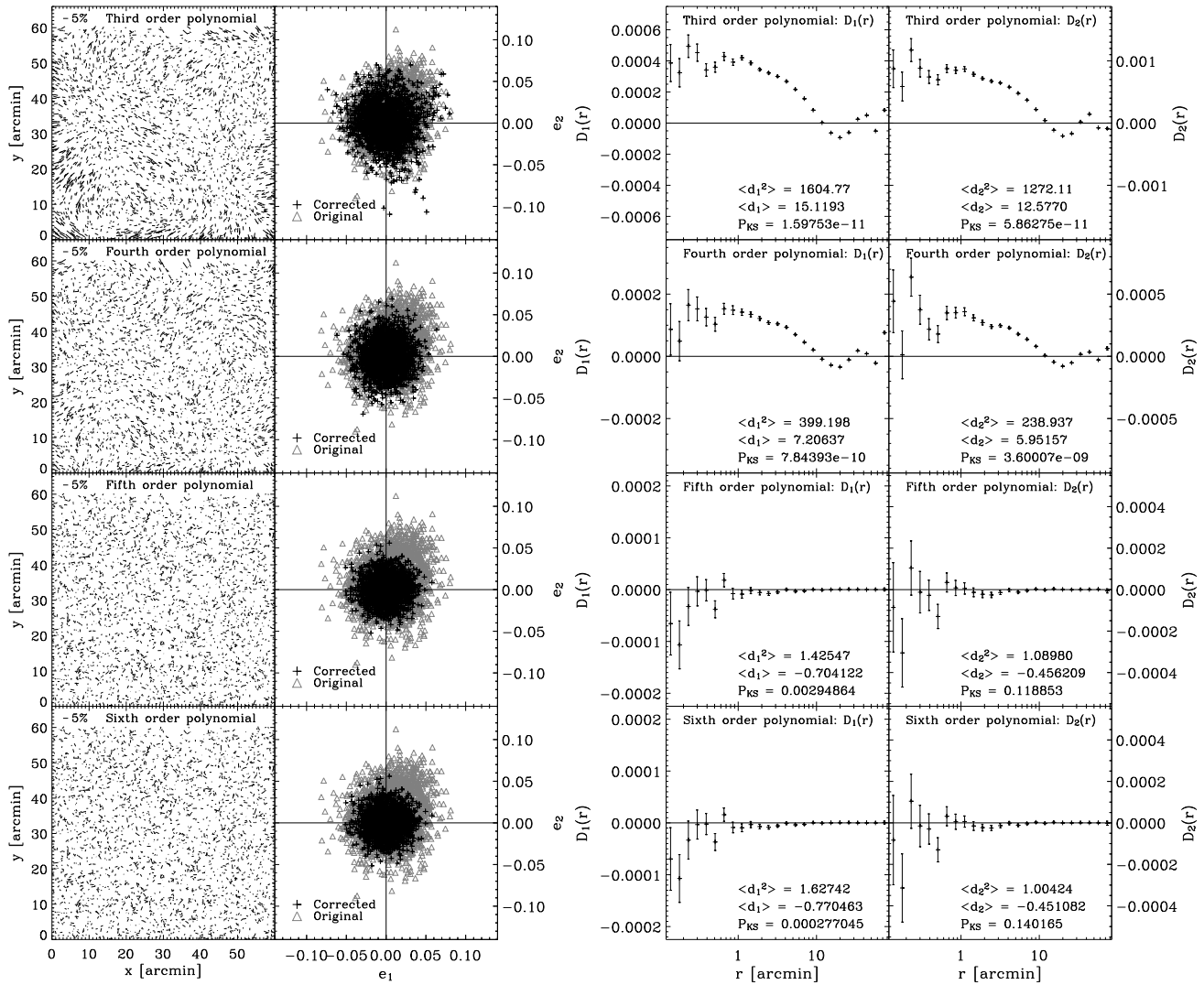


Figure 4. Traditional weak lensing tools for displaying the starfield PSF model fit results (left panels) and the corresponding $D_1(r)$ and $D_2(r)$ diagnostic correlation functions (right panels). As described in Section 3.1, the input PSF anisotropy e_t was a fifth order bivariate Chebyshev polynomial surface in each component of ellipticity.

Examining first the global fit results shown in Figure 4 it can be seen that both $D_1(r)$ and $D_2(r)$ show clear residual positive and negative correlations for the underfitting models, as predicted. Both diagnostics appear to be broadly consistent with zero for the fifth and sixth order fits. For the chipwise fits of Figure 5 the results are similar but show an interesting extra feature. While both diagnostics rule out a first order chipwise fit as clearly underfitting, and the second order more marginally, the third order chipwise fit shows slight evidence of anticorrelation on small scales. This is then seen more clearly when the fit is taken to sixth order chipwise, particularly for the $D_1(r)$ diagnostic. These results suggest an overfit to the data for third and sixth order chipwise fits, at least according the reasoning presented in Section 2.4: this is a reasonable conclusion given knowledge of the number of degrees of freedom in the initial model, and could not have been so easily diagnosed using current methods.

Furthermore, the fact that neither the second nor third order chipwise fits show perfect consistency with zero suggests that *none* of the schemes chosen in this artificial chipwise splitting of the

field is best suited to modelling the data, also a reasonable conclusion. However, it may be that this apparent inconsistency is instead caused by chance and the fact that $\langle m^*m \rangle(r)$ is no longer isotropic, since the artificial chips are rectangular. Nonetheless, even the possibility that $D_1(r)$ and $D_2(r)$ might allow general modelling schemes to be iteratively improved by correcting flaws such as the wrong choice of fitting function family, or the unnecessary splitting into independent chips, is of practical interest when fitting to an e_t of unknown functional form. Fitting to an arbitrary underlying field using a ‘wrong’ (or, more accurately, incomplete) basis will be explored further in Section 5, in which polynomial fits will be made to randomly generated fields with only an average power spectrum specified.

In summary, for the simple example presented in Figure 4, it appears that the degree of agreement with $D_1(r) = D_2(r) = 0$ is a potentially useful aid to model selection when compared with simple diagnostic tools that have been used in the past. In Figure 5 both diagnostics help rule out models that would clearly be under- or overfitting, but there is no scheme that performs perfectly once

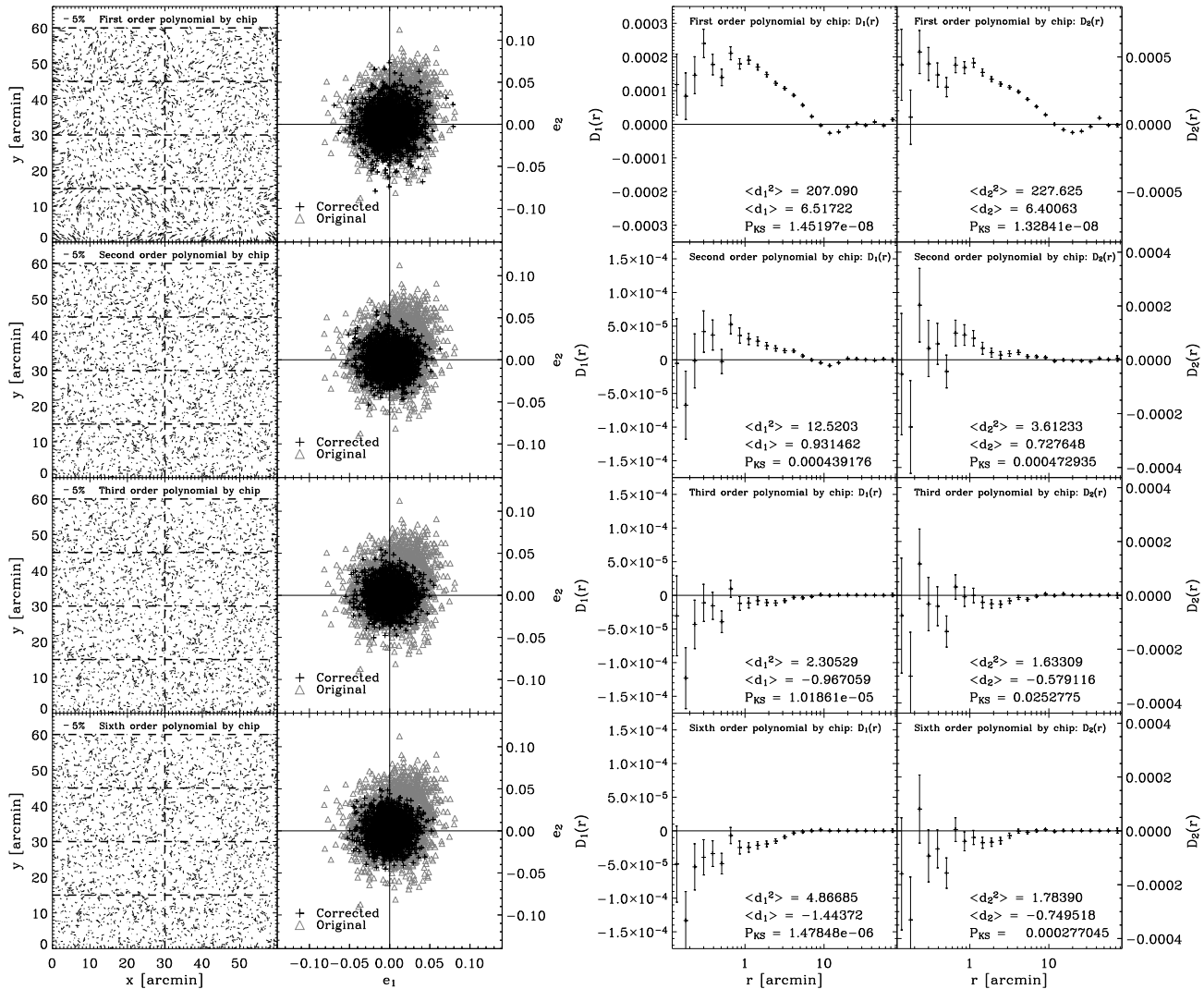


Figure 5. Traditional weak lensing tools for displaying the starfield PSF model fit results (left panels) and the corresponding $D_1(r)$ and $D_2(r)$ diagnostic correlation functions (right panels). These results are for the independent chipwise fits to each of the eight chip regions in the starfield. As described in Section 3.1, the input PSF anisotropy e_t was a fifth order bivariate Chebyshev polynomial surface in each component of ellipticity.

the field is artificially split into chips. This fact gives hope that correlation analyses of this sort might guide, in a directed manner, iterative improvements to modelling where there is no clear physical motivation for selecting a given scheme (in the case presented it might motivate the decision not to model chipwise, for example). It is now instructive to compare the results of this analysis with the more complex diagnostics of PSF modelling that have been discussed in the literature, which are also based upon correlations in residuals, to see what may be added by the approach presented here.

3.4 Comparison with the aperture mass dispersion and other related correlation diagnostics

The use of residual correlation diagnostics in a similar form to $D_1(r)$ and $D_2(r)$ is not new, having been advocated by Hoekstra (2004) in the form of the aperture mass dispersion estimator $\mathcal{M}(r)$ defined in equation (16) of Schneider et al. (2002) (see also Crittenden et al. 2002; Schneider, Van Waerbeke & Mellier 2002),

a filtered combination of $\xi_+(r)$ and $\xi_-(r)$ that gives an unbiased estimator of the cosmological aperture mass dispersion:

$$\langle M_{\text{ap}}^2 \rangle(r) = \frac{1}{2} \int \frac{r' dr'}{r^2} \left[\xi_+(r') T_+ \left(\frac{r'}{r^2} \right) + \xi_-(r') T_- \left(\frac{r'}{r} \right) \right] \quad (37)$$

and

$$\langle M_{\perp}^2 \rangle(r) = \frac{1}{2} \int \frac{r' dr'}{r^2} \left[\xi_+(r') T_+ \left(\frac{r'}{r^2} \right) - \xi_-(r') T_- \left(\frac{r'}{r} \right) \right], \quad (38)$$

where the functions $T_{\pm}(x)$ are non-zero only for $x < 2$ and are given in Schneider, Van Waerbeke & Mellier (2002). The aperture mass dispersion has the useful property that it allows a decomposition into ‘E’ and ‘B’ mode contributions (which are $\langle M_{\text{ap}}^2 \rangle(r)$ and $\langle M_{\perp}^2 \rangle(r)$ respectively) to the correlation signal, the former of which only is produced by a simple scalar mass potential (although B-modes can be created by contamination to the shear correction, intrinsic alignments of source galaxies etc., see Schneider 2006). This measure was then employed by Van Waerbeke et al. (2005) and Hoekstra et al. (2006) to find optimal schemes for mod-

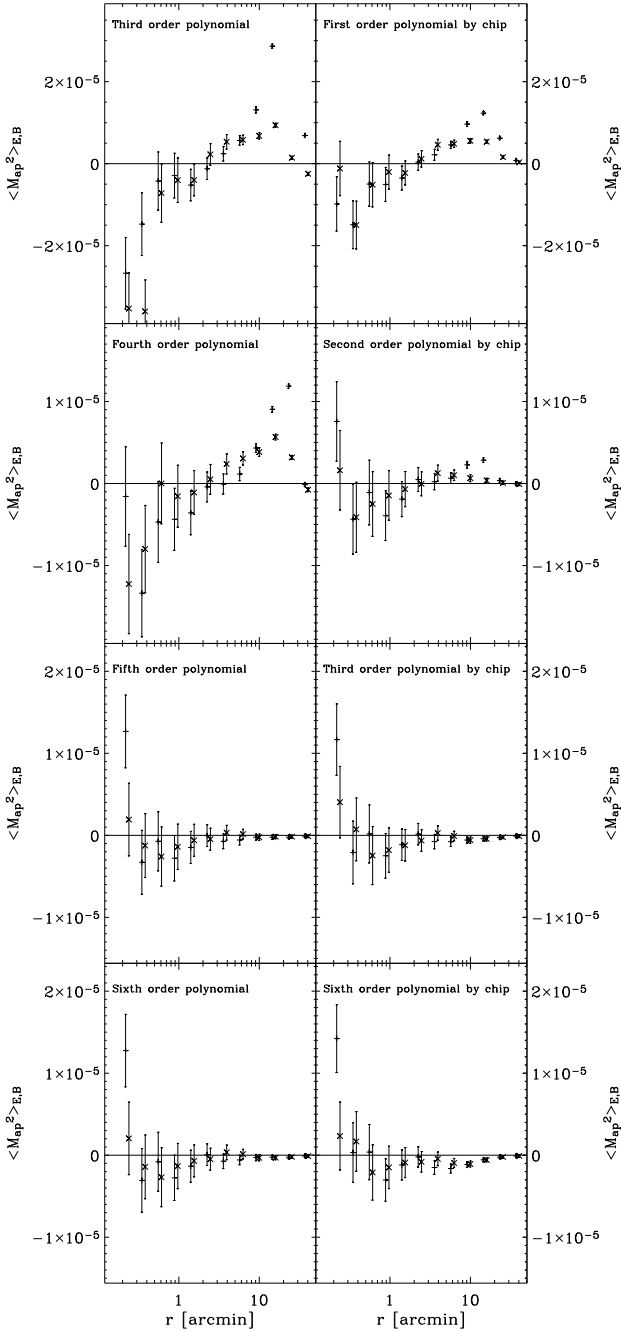


Figure 6. Aperture mass dispersion statistic for the residuals of the fits in Sections 3.2 & 3.3, corresponding to the diagnostics plotted in Figures 4 & 5. The crosses resembling addition signs represent the E mode signal and those resembling multiplication signs the B mode signal, which are offset slightly along the abscissa for clarity. Left hand side panels are for the simple polynomial fits to the whole field, whereas the right hand side panels show the dispersion in the chipwise fit residuals.

elling the spatial variation of the PSF anisotropy, aiming towards $\mathcal{M}(r) = 0$ for the residuals between modelled and measured PSF anisotropies. In both studies the chosen PSF fitting scheme was that which minimized the aperture mass dispersion of its residuals.

In Figure 6 the aperture mass dispersion is plotted for the residuals of the fits described in Sections 3.2 & 3.3, correspond-

ing to the diagnostics plotted in Figures 4 & 5. The results are similar to those of $D_1(r)$ and $D_2(r)$, in that there are clear correlations for the underfitting cases. The signal to noise is reduced, a known feature of this statistic (e.g., Hoekstra et al. 2006; Schneider 2006; Fu et al. 2008), and a means of positively identifying overfitting versus underfitting is less clear. This is because the aperture mass filtering of $\xi_+(r)$ and $\xi_-(r)$, which provides a desirably clean statistic when considering lensing due to physical mass distributions, makes the interpretation of correlated modelling residuals (via simple arguments such as those presented in Section 2) more complicated. One can say that correlation or anticorrelation exists, but saying which and why is less clear.

There is a suggestion in the bottom right hand side panel of Figure 6, for the sixth order chipwise fit, that the negative values of $\langle M_{ap}^2 \rangle_{E/B}$ are an indication of the overfitting model in the same way as the negative values of $D_1(r)$ and $D_2(r)$ at small scales; although with apparently less overall signal than $D_1(r)$. Justifying this hypothesis using extensions to the arguments of Section 2 may be possible, and would immediately identify a clearly overfitting PSF model in the study performed by Hoekstra et al. (2006) (Figure 7 of that work): a not impossible finding given their independent fitting of second order polynomials to each of 36 chips across the CFHTLS Megacam field. Whether this sheds more insight than $D_1(r)$ and $D_2(r)$ upon the PSF model quality is unclear, however, and even unlikely given the lower signal to noise of the aperture mass measures (although see Fu & Kilbinger 2009).

Nevertheless, as $\langle M_{ap}^2 \rangle$ (or the more recently-derived ring statistics $\langle \mathcal{R} \mathcal{R} \rangle_{E/B}$, see Schneider & Kilbinger 2007; Eifler, Schneider & Krause 2009; Fu & Kilbinger 2009) provides a model-independent method for E/B mode decomposition, it is in many ways a preferred choice for constraining cosmological parameters. Therefore, it will undoubtedly be of use to express residual correlations in the PSF model in terms of such quantities to quantify the contamination to the measured shear signal (e.g., Hoekstra 2004; see also Section 6). But in the diagnosis of poor modelling, and in the directed manner in which simplifications or increases in complexity to the PSF model can be motivated, the interpretability of $D_1(r)$ and $D_2(r)$ is an advance upon the use of the aperture mass dispersion.

Schrabback et al. (2007) also present a residual correlation analysis as a diagnostic of PSF modelling. These authors demonstrate that their chosen PSF model minimized the two functions $|\xi_+(r) + \xi_-(r)|$ and $|\xi_+(r) - \xi_-(r)|$ when measured upon model-data stellar ellipticity residuals, after randomly drawing stars from dense stellar fields (estimating the impact upon cosmic shear by scaling to an equivalent shear correction using randomly-drawn P^g values from a galaxy population; see Schrabback et al. 2007). Overfitting was not a concern for these authors, who built a family of robust and detailed *HST* PSF models using dense stellar fields and then selected from this family via a maximum-likelihood match to the far fewer stars available in the galaxy survey images. As such, no attempt was made to interpret the sign of the resulting functions and the absolute values alone sufficed as a diagnostic. Again, the interpretability of $D_1(r)$ and $D_2(r)$ in terms of over- and underfitting, via the arguments in Section 2, is of significant additional value.

3.5 Quantifying the agreement with $D_1(r) = D_2(r) = 0$

These results are interesting, but in order to test their repeatability it will be necessary to find some method of compressing the data and

quantifying the qualitative visual appraisal so far conducted. Ideally there would be a means of ascribing a single, easily-calculated number to the $D_1(r)$ and $D_2(r)$ results, describing how well a given model matches the desired $D_i(r) = 0$ behaviour. An obvious example is a chi-squared-like measure, but a true chi-squared is impossible without knowledge of the covariance between bins of $D_i(r)$, and these covariance matrices may in general only be estimated *post hoc* (often imperfectly) via a statistical jackknife or bootstrap. The calculation of even a single $D_1(r)$ or $D_2(r)$ takes some short time, varying with the square of the number of data points, and so these processor-intensive bootstrap techniques quickly become prohibitively expensive. In this Section we examine practical possibilities for a cheaper alternative to a full chi-squared measure of the $D_i(r) = 0$ hypothesis.

To assign simple numbers to these results, in effect searching for a better proxy to the ‘appraisal-by-eye’ performed in the previous Section, the following quantities are defined:

$$(d_i)_j = \frac{D_i(r_j)}{\sigma_{D_i}(r_j)}, \quad (39)$$

$$\langle d_i \rangle = \frac{1}{N_{\text{bins}}} \sum_j (d_i)_j, \quad (40)$$

$$\langle d_i^2 \rangle = \frac{1}{N_{\text{bins}}} \sum_j (d_i)_j^2. \quad (41)$$

Here $i = 1, 2$ so as to specify the $D_1(r)$ or $D_2(r)$ diagnostic respectively, j denotes each discrete bin of angular scale r_j , and the error estimate on each $D_i(r_j)$ is denoted as $\sigma_{D_i}(r_j)$. As discussed above, it should be noted that the values for neighbouring bins of $D_i(r)$ are correlated and the uncertainties $\sigma_{D_i}(r_j)$ do not take this into account: it would thus be dangerous to associate equation (41) with any sort of true chi-squared measure of the goodness of fit to a desired $D_i = 0$ scenario.

However, use may be made of the fact that the correlation between bins for the diagnostics must be expected to be minimized for those successful models that approach $D_i = 0$: this can be simply argued by considering that m is expected to become approximately random in these cases. Also of use is the fact that the most important task at hand is merely to select a best-fitting model using a single number that quantifies this success. It might still be hoped that (40) and (41) are useful as a way of *ranking* competing models. The overall normalization of $\langle d_i \rangle$ and $\langle d_i^2 \rangle$ for failing cases would, when ranking, be less important than the relative normalization as compared to successful cases.

Another means of quantifying the agreement with $D_i(r) = 0$ is via the the Kolmogorov-Smirnov (KS) test (see, e.g., Press et al. 1992; Lupton 1993), suggested to the grateful author by the anonymous referee. In the null hypothesis of a well-fitting model we may approximate that the individual values of $(d_i)_j$ are each independently described by a Gaussian distribution with zero mean and unit variance. The maximal difference between the empirical cumulative distribution function (derived from the data) and the cumulative distribution function of the null hypothesis can then be used to assess the goodness of fit. The probability $P_{\text{KS}}(d_i)$ that the null hypothesis could produce at least the maximal difference seen may then be calculated from a series approximation to the Kolmogorov distribution (although note that the use of this distribution is not strictly accurate, given that the ‘data’ $(d_i)_j$ we use are derived quantities, and so this measure should be rightly interpreted only as an approximate guide; see Press et al. 1992).

The values of each of the $\langle d_i \rangle$, $\langle d_i^2 \rangle$ and $P_{\text{KS}}(d_i)$ statistics, for each fit to the starfield, are given in Figures 4 & 5. It would be

naively expected that the best fitting f_m would show minimum values of $\langle d_i^2 \rangle$ and $|\langle d_i \rangle|$, and a maximum $P_{\text{KS}}(d_i)$: this is seen in the case of $D_1(r)$, but the $D_2(r)$ results marginally favour the overfitting sixth order polynomial in this case. All statistics strongly rule out lower order fits. For the chipwise fits the situation is more complex, due to their being no fitting model which shows clear consistency with $D_i(r) = 0$. Second and third order fits are variously preferred. As discussed in Section 3.3, this is perhaps due to there being no f_m in this artificially split case that can reproduce all features of the ellipticity field without some overfitting redundancy.

All three statistics show some promise in being able to approximately describe the extent to which $D_i(r) = 0$. More sophisticated approaches could certainly be explored, particularly given the information regarding the expected signatures of under- and overfitting described in Sections 2.3 & 2.4. This extra information might be perhaps be used within a Bayesian framework to select models, particularly if the modeller wished to rule out either an under- or overfitting model at any cost. This may be fertile ground for future work, as it is clear that the three statistics $\langle d_i^2 \rangle$, $|\langle d_i \rangle|$, and $P_{\text{KS}}(d_i)$ were chosen above all for their immediate simplicity and clarity.

These results lead to the possibility of asking another question: can model selection via the statistics described here be successfully repeated for a variety of input e_t fields? A single example field is hardly strong evidence for the utility of $D_1(r)$ and $D_2(r)$ in more general cases, so many more fields must be tested. The broad success of the three simplifying statistics described in this Section offers hope that the author might be spared from the need to visually inspect many plots of $D_1(r)$ and $D_2(r)$, and avoid the inevitable subjectivity in such an approach. Moreover, the necessity and difficulty of performing a full and stable statistical jackknife calculation (in order to estimate covariances) may be avoided. The following Section tests the success of $\langle d_i^2 \rangle$, $|\langle d_i \rangle|$ and $P_{\text{KS}}(d_i)$ as criteria for correctly identifying appropriate modelling order using a large number of randomly generated e_t anisotropy fields.

4 MONTE CARLO TESTING USING A SUITE OF SIMULATED ANISOTROPY MAPS

The repeatability the results of Section 3, which hinted at the utility of $D_i = 0$ as a model selection criterion, will now be tested using a large number of simulated e fields. To test the model selection for input physical signals of varying spatial complexity, each component of the input e_t is modelled as an n th order bivariate Chebyshev polynomial surface as described by equation (35), where the upper limit of the double sum is now $j + k \leq n = 1, 2, \dots, 7$. For each n a suite of $N_{\text{MC}} = 500$ randomly generated starfields is then created using a procedure directly analogous to that described in Section 3.1. Then, for each of the 500 simulated starfields of a given input order n , a set of best-fitting models for the anisotropy map are constructed as described in Section 3.2; this time, however, a greater range of bivariate polynomial fitting schemes f_m are explored, ranging in fitting order from $m = 1, \dots, 7$.

The same process is also performed using the artificial chipwise division of the field of view when fitting. Finally, the resulting $D_1(r)$ and $D_2(r)$ statistics were calculated as described in Section 3.3 for each input order n and fitting order m , for each of the 500 random starfields, and the $\langle d_i^2 \rangle_{\text{min}}$, $|\langle d_i \rangle|_{\text{min}}$ and $P_{\text{KS}}^{\text{max}}(d_i)$ criteria discussed above were then used to select the most appropriate modelling order.

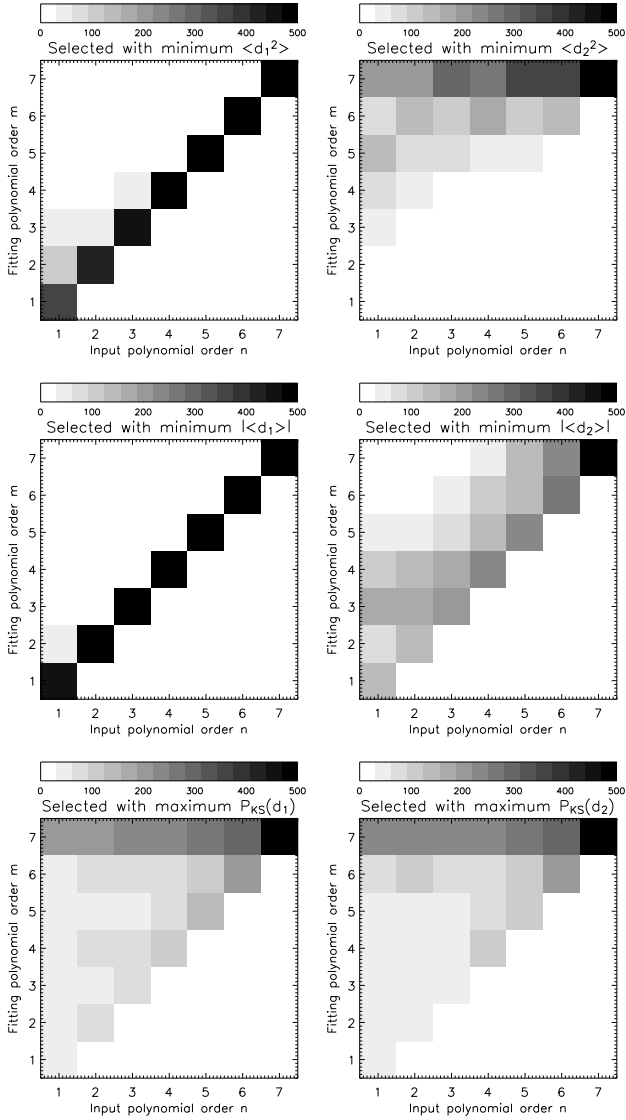


Figure 7. Number of model schemes selected as best fitting using the $\langle d_1^2 \rangle_{\min}$ (upper left), $\langle d_2^2 \rangle_{\min}$ (upper right), $|d_1|_{\min}$ (mid left), $|d_2|_{\min}$ (mid right), $P_{KS}^{\max}(d_1)$ (lower left) and $P_{KS}^{\max}(d_2)$ (lower right) criteria, as a function of input polynomial order n . The total number of fields simulated at each input order was $N_{MC} = 500$. Figures 7 & 8 were created using a modified version of the SHAPELETS_PLOT_IMAGE.PRO routine from the publicly-available *Shapelets* software (Massey & Refregier 2005).

4.1 Results

The number of times a global fitting scheme of order m was chosen as best representing the simulated starfield of input order n is shown in Figure 7, quantifying the success of the $\langle d_i^2 \rangle_{\min}$, $|d_i|_{\min}$ and $P_{KS}^{\max}(d_i)$ criteria for this simple Monte Carlo test. The same results are shown for the chipwise fits in Figure 8.

For the range of input models and statistics tested it appears that $D_1(r)$ is typically a cleaner and more reliable model selection diagnostic than $D_2(r)$, which in both the global and chipwise fits is noisier and appears to show a biased relative preference for overfitting models in most cases. $\langle d_1^2 \rangle_{\min}$ and $|d_1|_{\min}$ show striking success in selecting the correct fitting order in Figure 7, but not so their $D_2(r)$ counterparts. The performance of $P_{KS}^{\max}(d_i)$ is more disappointing overall and seems insensitive to identifying overfits

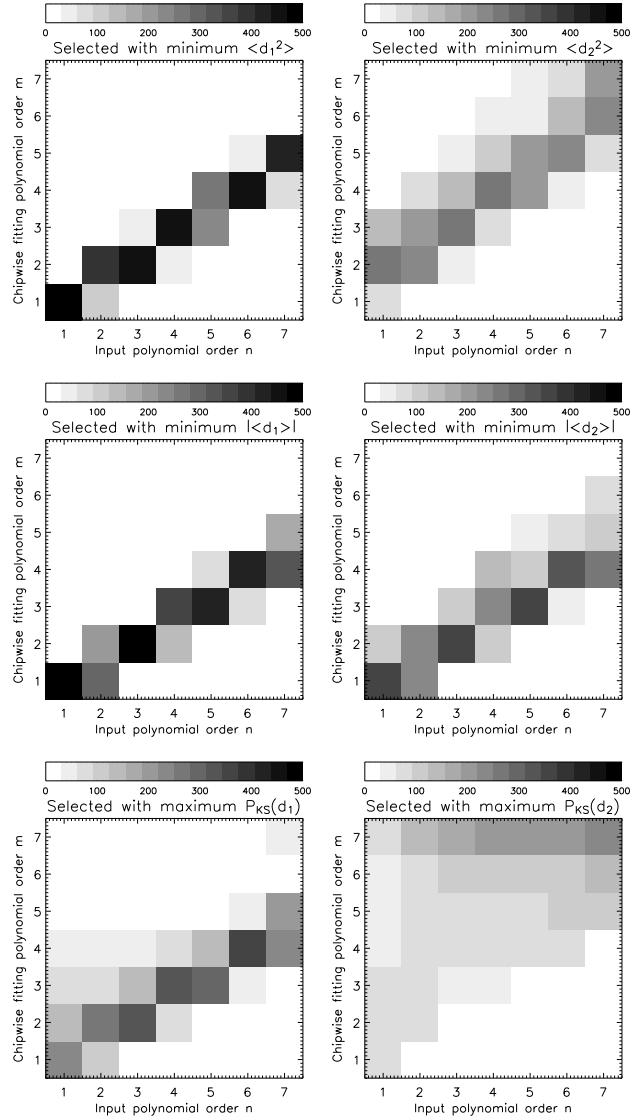


Figure 8. Number of chipwise model schemes selected as best fitting using the $\langle d_1^2 \rangle_{\min}$ (upper left), $\langle d_2^2 \rangle_{\min}$ (upper right), $|d_1|_{\min}$ (mid left), $|d_2|_{\min}$ (mid right), $P_{KS}^{\max}(d_1)$ (lower left) and $P_{KS}^{\max}(d_2)$ (lower right) criteria, as a function of input polynomial order n . The total number of fields simulated at each input order was $N_{MC} = 500$.

when fitting globally, although in Figure 8 there is evidence of it correctly ruling out the more extreme chipwise overfits, at least for $D_1(r)$. $|d_1|_{\min}$ appears to show moderate preference for lower order fits than $\langle d_1^2 \rangle_{\min}$, particularly at lower orders, perhaps due to the close cancelling of correlation and anticorrelation on different scales (c.f. Section 2.3). Nonetheless, all statistics appear to rule out underfitting models successfully.

The chipwise results show better rejection of overfitting models, and therefore greater overall agreement between the results for different statistics. This is not surprising when one considers that for chipwise fits the number of degrees of freedom in the fitting model increases more rapidly with increasing order m than in the global case. The comparison of the chipwise and global results therefore suggests that, for those statistics which failed to rule out overfits, the problem was more of relative sensitivity than a total failure. The $P_{KS}^{\max}(d_i)$ statistic performs the worst, and Press et al.

(1992) suggest a possible reason for this: the sensitivity of the KS test of deviations from the c.d.f. (d_i) is not independent of d_i , and is in fact most sensitive around the median value. This makes the test least sensitive in the wings of the probability distribution, and hence to the outliers which may give the clearest indication a poor fit. This is one plausible explanation, and Press et al. (1992) describe possible alternatives to the KS test that attempt to mitigate this problem. Another reason might be the incorrect use of the Kolmogorov distribution in the test, since $(d_i)_j$ are quantities derived from the data rather than direct data themselves (see Section 3.5; also Press et al. 1992).

These results leave open an avenue for potentially valuable further study, as an optimal way for identifying $D_1(r) = D_2(r) = 0$ is clearly not yet found. Despite this fact, the results of Figures 7 & 8 are extremely encouraging, for $\langle d_1^2 \rangle_{\min}$ and $|\langle d_1 \rangle|_{\min}$ in particular. The results $D_2(r)$ were generally less successful, and seemed to show an insensitivity to overfitting in particular. Possible reasons for this are now briefly discussed.

4.2 Understanding the relative failure of $D_2(r)$

In the Monte Carlo tests performed it appears that the selection criteria based upon $D_2(r)$ show some shortcomings that need to be explored. Firstly, they often prefer overfitting models when compared to the $D_1(r)$ results (biased when compared to the truth for Figure 7). Secondly, both $\langle d_2^2 \rangle$ and $|\langle d_2 \rangle|$ are noisy. This latter can perhaps be partially explained by the fact that $D_2(r)$ is itself often more noisy than $D_1(r)$, a natural consequence of the value and variation of e being typically larger than that of $e - e_m$ (see equations 13 and 14); the biased results warrant further investigation.

Complete answers as to why $D_2(r)$ performed relatively poorly in this simple experiment almost certainly lie outside the capability of this paper, as this behaviour may depend non-trivially upon many factors. Possible contributions could be: the number of stars simulated per field; the overall signal to noise for the e field; the geometry of the chosen field of view; the nature of the typical pattern described by the simulated e_t (the chosen polynomials, even when randomly generated, do not come close to being able to describe arbitrary surfaces); the degree of variance and covariance within and between bins of $D_2(r)$. Whilst all these factors may potentially be limiting in the correct circumstance, the last is worthy of some further discussion in particular as it is one aspect in which $D_2(r)$ may differ significantly from $D_1(r)$.

Evidence of overfitting is generally seen at small scales, and it has been seen that on large scales $D_i \simeq 0$ even for drastic overfits (e.g. Figure 5). At these scales the quoted errors upon $D_2(r)$ will still be large when compared to those for $D_1(r)$, because of the typically greater values of e as compared to $e - e_m$, meaning that contributions to $\langle d_2^2 \rangle$ on these scales are overly suppressed. Moreover, the use of $\langle d_i^2 \rangle$ as a means of ranking competing models will work best in situations where the covariance matrix is totally diagonal, and will correspond in such cases to a chi-squared-like measure of goodness of fit to $D_i = 0$. Conversely, strong off-diagonal values might produce exactly the results seen in Figures 7 & 8 for the $D_2(r)$ diagnostics. If false, the assumption of weakly correlated uncertainties between bins, which is implicit for the utility of $\langle d_i^2 \rangle$ and $|\langle d_i \rangle|$, will lend undue weight to the supposed success of $D_i = 0$ on large scales and therefore undue credence to the overfitting model itself. If the covariance matrix for $D_2(r)$ contains significant off-diagonal terms, even in the case of a successful model,

this may be cause for the systematic preference towards overfitting models seen in Figures 7 & 8.

In that case, however, it must also be seen if there is a systematic reason why the covariances of $D_1(r)$ and $D_2(r)$ differ in their diagonality. One important difference is apparent from the very definitions given in equations (13) and (14): the first diagnostic is the residual-residual autocorrelation, whilst the second is a measure of the data-residual cross-correlation. It may be that $D_2(r)$ will therefore suffer from strong covariances even for cases approaching $D_2(r) = 0$, due to the physically correlated nature of the data e , whereas such correlations in $D_1(r)$ will inevitably decrease as the model tends towards $D_1(r) = 0$. Another difference may lie in the angle averaging, performed over all pairs separated by distance r , implicit in the definition of the correlation functions thus far used in this paper (see, e.g., equations 3 and 5). It can be imagined that $D_2(r)$, being more strongly dependent upon the non-isotropic field e_t , might suffer from greater uncertainty and even bias due to the angle averaging that is implicit in the way $D_1(r)$ and $D_2(r)$ are calculated.

These are plausible explanations for the effects seen but, unfortunately, this discussion will remain essentially un-concluded without further investigation. Estimating *post hoc* the covariance matrices of correlation functions such as $D_2(r)$ is expensive with current computing resources and, as the covariance of $D_2(r)$ will depend non-trivially upon the starfield e_t , the calculation would need to be made many times within the current simulation framework. Pessimistically, even with such work we may in fact be learning more about the properties of any simulated e_t than about $D_i(r)$. Despite these issues regarding $D_2(r)$, it has certainly been demonstrated that both $D_i(r)$ show some potential for diagnosing modelling quality, and that $D_1(r)$ appears outstandingly successful in the tests so far conducted. A next step is to enlarge the space of potential e_t fields to include more general, arbitrary structure, and to see how $D_1(r)$ and $D_2(r)$ perform when a perfect fit may no longer be possible.

5 FITTING ARBITRARY SPACIAL PATTERNS

So far in this paper the testing of the $D_1(r)$ and $D_2(r)$ diagnostics has been for cases in which a perfect fit to the data was possible at some modelling order. The chipwise fitting made the situation somewhat interesting by balancing this against an increased propensity to overfit: for example, whilst it might be necessary to fit a fifth order polynomial chipwise to formally recover *all* aspects of an underlying fifth order global e_t , it may not always be justified by the data available. This was reflected in the results of Figure 8, which preferred lower order chipwise fits even though such models might not be able to perfectly reproduce all aspects of the input PSF variation. In this Section we take the analysis one step further by introducing more arbitrary spacial patterns, to see whether the diagnostics can differentiate between more general variation in the degree of spatial structure.

Once again a Monte Carlo approach is taken and we build three suites of $N_{MC} = 500$ randomly generated starfields. For each field, each component of the underlying e_t is modelled as a Gaussian random field with a specified average power spectrum. These can be constructed by summing random phase Fourier modes across the 1 deg^2 field of view

$$(e_t)_i = \sum_{n,m=1}^{N_{\text{limit}}} c_{nm} \cos(k_n x + \phi_n) \cos(k_m y + \phi_m), \quad (42)$$

where $k_n = n\pi \text{ deg}^{-1}$, and $i = 1, 2$ denotes the real and imaginary parts of e_t respectively. The value $N_{\text{limit}} = 300$ was chosen to ensure that structure was fairly represented well below the typical separation for 2500 objects in a 1 deg^2 field ($1/50 \text{ deg}$), although this slowed the field generation somewhat. ϕ_n and ϕ_m are chosen to be random uniform variables in the range $[0, 2\pi]$ and, having defined $k^2 = k_n^2 + k_m^2$, the coefficients c_{inm} are then drawn from Gaussian random variables of zero mean and variances satisfying the constraint that the ensemble average power spectrum is given by a power law

$$\langle c_{inm} c_{in'm'} \rangle = Ak^{-\alpha} \delta_{nn'} \delta_{mm'}. \quad (43)$$

For each of the three Monte Carlo starfield suites, different choices were made for the value of the power law slope α : 11/3 and 11/6 (motivated by the Kolmogorov spectrum for atmospheric turbulence, e.g. Sasiela 1994, relevant for ground-based lensing), and the intermediate value 11/4. For each α the normalization A was accordingly set so as to give equal power in the lowest order mode, specifically setting $\sqrt{\langle c_{i11}^2 \rangle} = 0.01$. This normalization, once stellar ellipticities were sampled at 2500 randomly-distributed points and a Gaussian noise of $\sigma_N = 0.015$ added to each component (c.f. Section 3.1), once more recreated simulated starfields of realistic anisotropy for the CFHTLS-W.

As in Section 4, these simulation starfields were then fit using simple bivariate polynomials of order $1, \dots, 7$, globally. The $D_1(r)$ and $D_2(r)$ statistics were calculated for each fitting order, and the $\langle d_i^2 \rangle_{\min}$, $|d_i|_{\min}$ and $P_{\text{KS}}^{\max}(d_i)$ criteria used to select the most appropriate fitting model. The results of these fits for $D_1(r)$ and $D_2(r)$ can be seen in Figures 9 & 10, respectively.

Most importantly, there are clear differences in the distribution of preferred fitting order as a function of power spectrum slope: as would be hoped the shallowest $\alpha = 11/6$ case systematically prefers the highest order fits, suggesting even that higher than seventh order fits might be necessary in many of the starfields. The $\alpha = 11/4, 11/3$ cases peak lower (except for $P_{\text{KS}}^{\max}(d_i)$, which performs poorly again), with the steepest power spectrum preferring the lowest order fits. The $\langle d_i^2 \rangle_{\min}$ and $|d_i|_{\min}$ measures all seem to be able to differentiate well between the degrees of spatial structure in these arbitrary underlying models. The tendency for $|d_i|_{\min}$ to prefer lower order fits than $\langle d_i^2 \rangle$ is seen again, as is the tendency for $D_2(r)$ to prefer higher order fits relative to $D_1(r)$. It should be noted that this latter behaviour is strikingly modest when compared to the results of Section 4, perhaps due to a lesser degree of spatial correlation in the randomly-generated underlying e_t (see discussion in Section 4.2).

The results of Figures 9 & 10, when taken alongside those for the polynomial starfields of Section 4, give compelling evidence for the utility of $D_i(r)$ as diagnostic tools for PSF modelling. Here we have shown that they are able to discriminate between physical systems of varying complexity despite unknown or arbitrary underlying forms, and in Section 4 it was shown that when the model approaches the ‘correct’ form this too can be identified. From simple arguments the diagnostics provide a way of making directed, iterative, and possibly automated improvements to both modelling accuracy and stability. Whilst the three descriptive statistics suggested in Section 3.5 remain imperfect in many aspects, there is scope for improving them. All of this offers hope that $D_i(r)$ will be a useful tool for systematically improving PSF modelling in future weak lensing studies. With this in mind, we now turn to a brief discussion of how these diagnostics may be related to requirements for cosmic shear measurement accuracy.

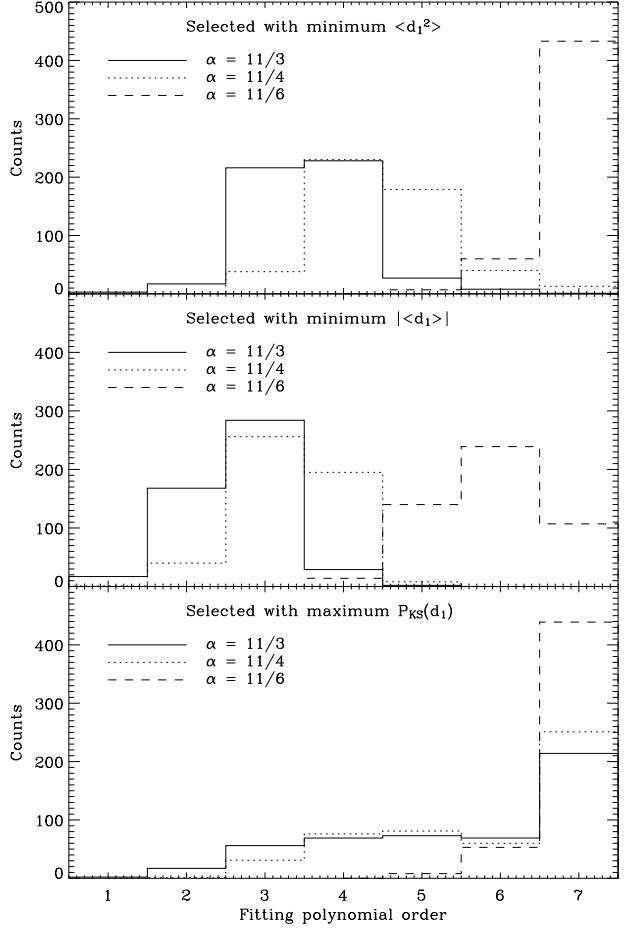


Figure 9. Number of model schemes selected as best fitting using the $\langle d_1^2 \rangle_{\min}$ (upper panel), $|d_1|_{\min}$ (middle panel), and $P_{\text{KS}}^{\max}(d_1)$ (lower panel) criteria, as a function of the input e_t power spectrum slope α . The total number of fields simulated for each input power spectrum was $N_{\text{MC}} = 500$.

6 RELATION TO COSMIC SHEAR PREDICTIONS

The results presented so far in this paper compare various fitting models, but no attempt has been made to propagate these results through to the impact upon cosmic shear measurements. In this Section we describe relevant results in the literature, and show how these allow values of $D_1(r)$ in particular to be related to the impact upon cosmic shear systematics. This will be necessary to help define the limits and requirements for the quality of PSF modelling for future surveys. $D_2(r)$ is less useful in this respect as it cross-correlates the modelling residuals with the telescope PSF e variation, a filtering that on average will be unmatched to any cosmic signal.

In what follows significant use is made of results from Paulin-Henriksson et al. (2008), adapted so to propagate the correlated effects of poor spatial modelling of the PSF variation into an impact upon measurements of cosmic shear. These authors use a simple description based upon unweighted image moments to argue that, to first order in the quantities concerned, the systematic error δe^{sys} upon a measured galaxy ellipticity will be given by

$$\delta e^{\text{sys}} \simeq (e_{\text{gal}} - e_{\text{PSF}}) \frac{\delta R_{\text{FSF}}^2}{R_{\text{gal}}^2} - \left(\frac{R_{\text{PSF}}}{R_{\text{gal}}} \right)^2 \delta e_{\text{PSF}} \quad (44)$$

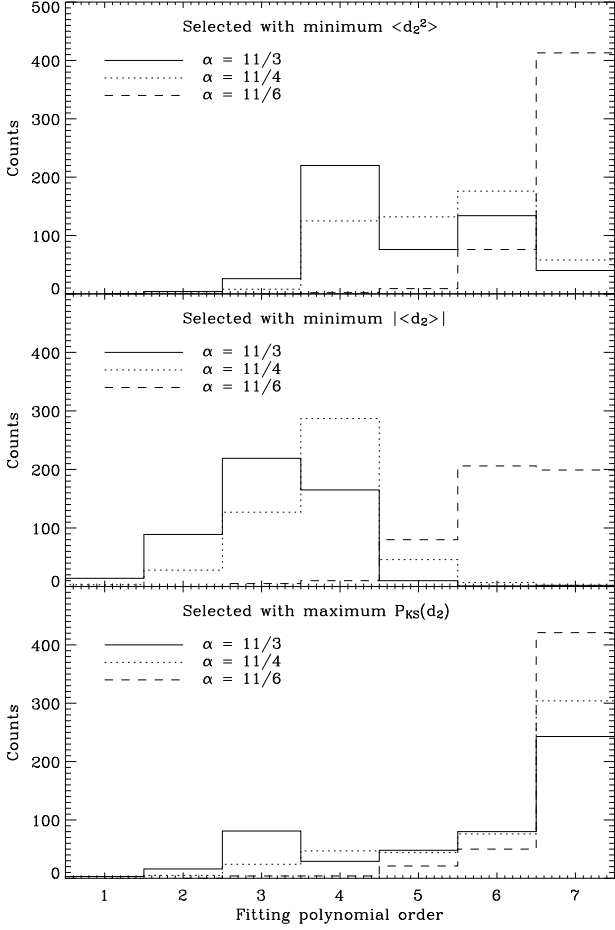


Figure 10. Number of model schemes selected as best fitting using the $\langle d_2^2 \rangle_{\min}$ (upper panel), $| \langle d_2 \rangle |_{\min}$ (middle panel), and $P_{KS}^{\max}(d_2)$ (lower panel) criteria, as a function of the input e_t power spectrum slope α . The total number of fields simulated for each input power spectrum was $N_{MC} = 500$.

where e_{gal} and e_{PSF} are the ellipticity of the galaxy and the PSF in this region of sky, R_{gal} and R_{PSF} are the respective angular radii. δR_{PSF}^2 and δe_{PSF} represent uncertainties in these aspects of the PSF due to poor or unstable modelling. Changing to the notation of Section 2, δe_{PSF} can be immediately identified with the modelling inaccuracy m . Considering only the second term (as the D_i diagnostics cannot directly shed light on δR_{PSF}^2) we may write the associated error in the measured shear due to the poorly modelled PSF anisotropy as

$$\delta\gamma^{sys} \simeq -\frac{m}{P^\gamma} \left(\frac{R_{PSF}}{R_{gal}} \right)^2, \quad (45)$$

having defined the shear susceptibility factor P^γ as in Paulin-Henriksson et al. (2008) (these authors take a value of $P^\gamma \approx 1.84$ as typical for a distribution of measured galaxy ellipticities). The measured shear for a region of sky may be then written as $\gamma = \gamma_t + \delta\gamma^{sys} + \delta\gamma^N$, where γ_t is the ‘true’ shear and $\delta\gamma^N$ is a random, assumed-unbiased noise term. Using the expression (3) to define a shear correlation ξ_+^γ and taking equation (45) together with the inequality (33), we may approximate the systematic impact due

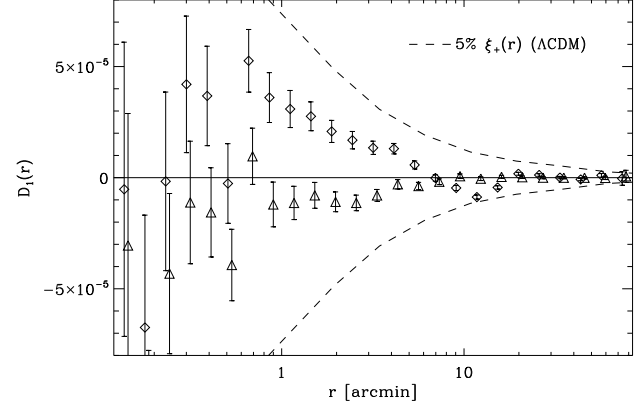


Figure 11. $D_1(r)$ fitting results for the second order (squares) and third order (triangles) chipwise fits to the starfield of Section 3 (reproduced from Figure 5). Overlaid with the dashed line is the tolerance on $D_1(r)$ that must be met to ensure that systematic errors due to PSF variation to contribute less than 5% of the Λ CDM cosmological ξ_+^γ signal for source galaxies at redshift $z = 0.7$, calculated as described in Section 6.

to a poorly modelled PSF anisotropy as

$$|\delta\xi_+^\gamma|^{sys}(r) \equiv | \langle \gamma^* \gamma \rangle (r) - \langle \gamma_t^* \gamma_t \rangle (r) | \quad (46)$$

$$= \left| \frac{\langle m^* m \rangle (r)}{(P^\gamma)^2} \left\langle \left(\frac{R_{PSF}}{R_{gal}} \right)^4 \right\rangle \right| \quad (47)$$

$$\leq \left| \frac{D_1(r)}{(P^\gamma)^2} \left\langle \left(\frac{R_{PSF}}{R_{gal}} \right)^4 \right\rangle \right|. \quad (48)$$

Following the arguments of Section 2.4, the last expression will tend towards an identity for underfitting models but place an upper limit on the systematic contribution from m in the overfitting case.

The expression (48) can also be reversed to define a tolerance limit upon $D_1(r)$ for a given ‘acceptable’ level of systematics when fitting models to the spatial variation of the PSF. Paulin-Henriksson et al. (2008) argue that the steepness of the galaxy size distribution justifies the approximation that, typically,

$$\left\langle \left(\frac{R_{PSF}}{R_{gal}} \right)^4 \right\rangle \simeq \left[\left(\frac{R_{PSF}}{R_{gal}} \right)_{\min} \right]^4 \simeq (1/1.5)^4; \quad (49)$$

together with $P^\gamma \simeq 1.84$ this allows limits to be placed upon acceptable values of $D_1(r)$, relative to the expected cosmological signal $\xi_+^\gamma(r)$. Using these values, Figure 11 shows the tolerance upon $D_1(r)$ that must be met to ensure that anisotropy systematics do not exceed 5% of the Λ CDM cosmological signal on any scale for a population of lensing source galaxies at $z = 0.7$ (a typical median value for current and planned wide-area lensing surveys such as CFHTLS-W and Pan-STARRS: e.g. Fu et al. 2008; Hoekstra et al. 2006; Kaiser 2004). This prediction was calculated using the Smith et al. (2003) non-linear matter power spectrum for a flat, Λ CDM cosmology with $\Omega_m = 0.25$, $\Omega_\Lambda = 0.75$, $h = 0.7$, power-law spectral index $n_s = 1$ and normalization $\sigma_8 = 0.8$. Over-plotted are the second and third order chipwise fitting results of Section 3 and Figure 5.

The arguments presented here are relatively simplistic, and the impact of residual PSF anisotropy variation upon shear estimation will also generally depend upon the correction method used. However, the approximate tolerance limits they place upon the quality of PSF modelling are a useful first guide, and the accuracy of these

limits could easily be improved further by simulating erroneous PSF correction through any given shear measurement pipeline.

7 GENERAL MODELLING APPLICATIONS

A final question is whether the technique can be extended into spheres beyond the characterization of anisotropic PSFs for weak lensing. Another possible application of the analysis, also within the weak lensing context, is illustrated by Figure 12. Here a shapelet model of a galaxy, imaged in the F606W band of the *Hubble Space Telescope* Ultra Deep Field (Beckwith et al. 2006), can be seen compared to the original image and to the map of residuals between the two; the shapelet decomposition was performed using the publicly available code described by Massey & Refregier (2005). The residual map clearly shows correlated features but, despite this, the galaxy image passed through the automated, iterative fitting routine of Massey & Refregier (2005) without any error error flags. Moreover, the model passed with a reasonable reduced chi-squared of $\chi^2 = 1.02087$ as compared to a good fit-expected value of $\chi^2 \simeq 1 \pm 0.0165$, calculated via the 3657 degrees of freedom in the model (number of pixels minus number of model coefficients). In fact, this low value of chi-squared may be sensitive to an erroneous overestimation in the automatic calculation of the background sky noise used by the shapelet software, but this simply highlights an important limitation of such techniques when the uncertainty in the data is but imperfectly known. The diagnostic tools presented here are less sensitive to ignorance about the uncertainty on individual measurements, and may be used even in the total absence of such knowledge.

Thus motivated, a simple generalization of the technique into other potential applications is now discussed in brief. The correlation of two complex functions f and g in an n -dimensional space can be defined as

$$[f \star g](\mathbf{r}) \equiv \int_{\mathbb{R}} f^*(\mathbf{x})g(\mathbf{x} + \mathbf{r})d^n x. \quad (50)$$

In the case of the correlation functions defined in Section 2.1, f and g would be formed from simple combinations of the e_{tan} and e_{\times} quantities defined by equation (4). Once more, a general function $g(\mathbf{x})$ may be defined as a field that describes a number of discrete, noisy samplings of an underlying ‘true’ field $g_t(\mathbf{x})$; this quasi-field represents the measurements:

$$g(\mathbf{x}) = g_t(\mathbf{x}) + N(\mathbf{x}). \quad (51)$$

As before, N will be assumed to be stochastic noise. Similarly, a model fit to these measurements can be written as

$$g_m(\mathbf{x}) = g_t(\mathbf{x}) + m(\mathbf{x}, g_t, N; f_m) \quad (52)$$

where m is again the inaccuracy and f_m labels the modelling scheme chosen to represent $g(\mathbf{x})$.

As in Section 2.1, a starting point is to then make simple assumptions about the properties of the noise for the data being considered, namely that

$$[N \star N](\mathbf{r}) = \int_{\mathbb{R}} N^*(\mathbf{x})N(\mathbf{x} + \mathbf{r})d^n x = 0 \quad (53)$$

and

$$[g_t \star N + N \star g_t](\mathbf{r}) = 0. \quad (54)$$

Given these assumptions, and in direct analogy to the functions defined in Section 2.2, the following two diagnostic functions can be

defined in general:

$$D_1(\mathbf{r}) \equiv [(g - g_m) \star (g - g_m)](\mathbf{r}) \quad (55)$$

$$= [m \star m](\mathbf{r}) - [m \star N + N \star m](\mathbf{r}), \quad (56)$$

$$D_2(\mathbf{r}) \equiv [g \star (g - g_m) + (g - g_m) \star g](\mathbf{r}) \quad (57)$$

$$= -[m \star g_t + g_t \star m](\mathbf{r}) - [m \star N + N \star m](\mathbf{r}). \quad (58)$$

These functions should tend to zero for all vectors \mathbf{r} if the model fit employed is both stable and accurate, and will have predictable behaviour for over- and underfitting models in a way directly analogous to the results of Sections 2.3 & 2.4. If the noise assumptions of equations (53) and (54) are broken then the functions above will be expected to be non-zero, but tending towards a form that may be derived from observations of pure noise.

The use of $D_1(r)$ and $D_2(r)$ may provide valuable clues to ways in which the modelling of galaxy images such as Figure 12 may be improved; one immediate example might be in the quantified selection of a more appropriate basis set than the Gauss-Hermite polynomials used by the shapelet method (Ngan et al. 2008). However, there is no reason why the method must be restricted to weak lensing analyses, as the quantification and suppression of correlated residuals is surely a justified concern wherever physical data is being described by a best fitting model. Correlations in residuals between neighbouring data points should be examined wherever best-fitting models are being used to represent physical data, including but not limited to CMB temperature power spectra, supernova distance-redshift curves, or determinations of the matter power spectrum from galaxy clustering. However, such matters are clearly a topic for further investigation; the overall findings and results of this work will now be discussed.

8 CONCLUSIONS

A simple theoretical framework for an interpretation of statistically correlated modelling residuals has been presented, and developed into a pair of independent two-point correlation function diagnostics for the specific application of PSF modelling in weak lensing. The $D_1(r)$ and $D_2(r)$ diagnostic functions have been defined as the autocorrelation in residuals and the data-residual cross-correlation, which should tend to zero on all scales for good models. Visual inspection of these functions has been shown to give sensitive insight into model selection for a single simulated starfield designed to mimic typical telescope PSF patterns. This visual inspection of the diagnostics not only quantifies the success of a given best fit model, but also provides improvements to be made in a directed fashion via the simple distinguishing features common to both underfitting ($D_i(r)$ expected to be both positive and negative as a function of r) and overfitting models ($D_i(r)$ negative only, most likely on small scales).

The analysis was then extended to a large suite of randomly generated starfields, and simple quantifications of the extent to which $D_1(r) = 0$ were shown to be able to select appropriate orders of modelling complexity very successfully. The results for $D_2(r)$ were less successful at this stage, but this may be partly explained by the greater covariance expected between neighbouring bins for this correlation function. For the arbitrary e_t fields of Section 5 the two performed more similarly, although with $D_2(r)$ still preferring slightly more complex fitting surfaces. Nonetheless, the success of the $D_1(r)$ diagnostic in particular provides strong evidence that the method may be used as a means of improving mod-

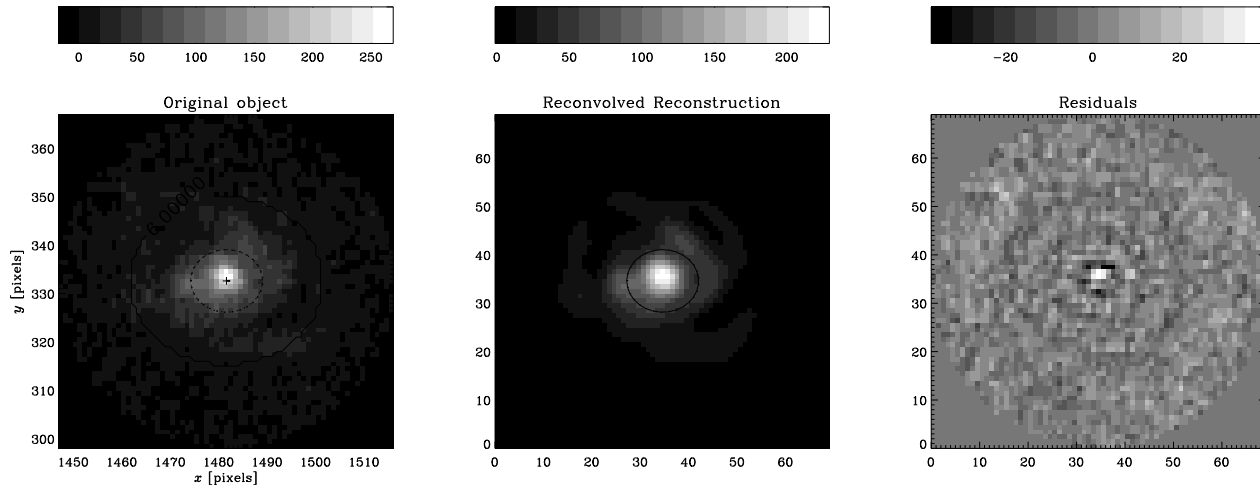


Figure 12. Galaxy image, model and residuals map for a galaxy from the F606W filter *Hubble* Ultra Deep Field (Beckwith et al. 2006). The image model and plots were made using the publicly-available *Shapelets* software (Massey & Refregier 2005). In this example the galaxy shape model passes through the automatic shapelet modelling process with no error flags, and a reasonable reduced χ^2 of 1.02087 (this is calculated using the individual pixel values, treating each pixel as independent and giving a total number of degrees of freedom of 3657).

els of the spatial variation of the PSF in weak lensing analyses. The diagnostics successfully differentiate the stability and accuracy of competing models in cases where the chosen fitting basis both can and cannot fully reproduce the underlying e_t . In cases where visual inspection and full covariance calculations are possible when making modelling choices, i.e. if $D_1(r)$ and $D_2(r)$ need not be calculated many times, both diagnostics may give useful insight into the properties of the model and scales on which the fit can be given greater or lesser freedom.

Such properties are clearly of great relevance to the analysis of forthcoming weak lensing surveys, and so simple arguments were given for how to relate the $D_1(r)$ diagnostic to precision requirements for the fundamental cosmic shear observable $\xi_+^{\gamma}(r)$. Finally, the start of a generalization of the technique into more wider modelling applications was discussed. This simple work gives hope that the technique might be of use in spheres outside weak lensing.

However, the description presented is basic, largely empirical, and leaves many questions unanswered. Placing the analysis of the D_1 and D_2 diagnostics on a truly statistical level, by truly estimating the *probability* of a given $D_i(r)$ in the null hypothesis of a well-chosen model, would be a topic for useful future investigation. The KS test analysis attempted in this respect clearly falls somewhere short of this aim. Such analysis may inevitably be much restricted by assumptions that will need to be made about the properties of the noise upon data and, perhaps less tractably, the properties of the underlying physical reality $g_t(x)$ that is being modelled. Despite these difficulties, such work might allow the technique to do more than simply rank competing models by quantifying agreement with $D_i(r) = 0$, which is where the theory currently stands.

If a more complete statistical description can be achieved, the analysis of correlated modelling residuals may form an extremely useful addition to existing model selection criteria based upon calculations of the statistical likelihood, such as the AIC, BIC and Bayesian evidence. The technique requires little prior knowledge of the uncertainties upon individual data points, except for the simplifying approximation that they are random and uncorrelated, making it potentially more robust than chi-squared when uncertainties are difficult to estimate. Finally, the greatest interest in the technique

may lie in where it most differs from standard model selection criteria: the fact that it takes the relative locations of data points, as well as their data values, directly into account. This information is valuable, and efficient ways to make use of it may be possible.

9 ACKNOWLEDGMENTS

The author would like to thank David Bacon, Henk Hoekstra, Yannick Mellier, Tim Schrabback and Ludo van Waerbeke for useful comments and suggestions in the period leading up to this work. Martin Kilbinger must also be thanked for both useful discussions and for the use of his correlation function code, and the anonymous referee should also be thanked for their useful suggestions which significantly added to the breadth and detail of the paper. This work was performed in support of the CFHTLS Systematics Collaboration (Van Waerbeke et al., in prep.), and the author has been supported by an Experienced Researcher Fellowship from the European Union Dark Universe through Extragalactic Lensing (DUEL) Research Training Network.

This paper has been typeset from a \TeX / \LaTeX file prepared by the author.

REFERENCES

- Arfken G. B., Weber H. J., 2005, *Mathematical methods for physicists* 6th ed.
- Beckwith S. V. W., et al., 2006, *AJ*, 132, 1729
- Bernstein G. M., Jarvis M., 2002, *AJ*, 123, 583
- Bridle S., et al., 2008, *ArXiv e-prints: astro-ph/0802.1214*
- Crittenden R. G., Natarajan P., Pen U.-L., Theuns T., 2002, *ApJ*, 568, 20
- Efstathiou G., 2008, *MNRAS*, 388, 1314
- Eifler T., Schneider P., Krause E., 2009, *ArXiv e-prints: astro-ph/0907.2320*
- Fu L., et al., 2008, *A&A*, 479, 9

- Fu L., Kilbinger M., 2009, ArXiv e-prints: astro-ph/0907.0795
- Gelman A., Carlin J. B., Stern H. S., Rubin D. B., 2003, Bayesian Data Analysis, Second Edition. Chapman & Hall/CRC
- Heymans C., et al., 2005, MNRAS, 361, 160
- Heymans C., et al., 2006, MNRAS, 368, 1323
- Heymans C., et al., 2008, MNRAS, 385, 1431
- Hoekstra H., 2004, MNRAS, 347, 1337
- Hoekstra H., 2007, MNRAS, 379, 317
- Hoekstra H., Franx M., Kuijken K., Squires G., 1998, ApJ, 504, 636
- Hoekstra H., Hsieh B. C., Yee H. K. C., Lin H., Gladders M. D., 2005, ApJ, 635, 73
- Hoekstra H., Mellier Y., Van Waerbeke L., Semboloni E., Fu L., Hudson M. J., Parker L. C., Tereno I., Benabed K., 2006, ApJ, 647, 116
- Jarvis M., Jain B., 2004, ArXiv e-prints: astro-ph/0412234
- Jarvis M., Schechter P., Jain B., 2008, ArXiv e-prints: astro-ph/0810.0027
- Kaiser N., 2004, in J. M. Oschmann Jr. ed., Society of Photo-Optical Instrumentation Engineers (SPIE) Conference Series Vol. 5489 of Presented at the Society of Photo-Optical Instrumentation Engineers (SPIE) Conference, Pan-STARRS: a wide-field optical survey telescope array. pp 11–22
- Kaiser N., Squires G., Broadhurst T., 1995, ApJ, 449, 460
- Kurek A., Szydlowski M., 2008, ApJ, 675, 1
- Leauthaud A., et al., 2007, ApJS, 172, 219
- Liddle A., Mukherjee P., Parkinson D., 2006, Astronomy and Geophysics, 47, 040000
- Liddle A. R., 2007, MNRAS, 377, L74
- Lupton R., 1993, Statistics in theory and practice. Princeton, N.J.: Princeton University Press, —c1993
- Mandelbaum R., Seljak U., Kauffmann G., Hirata C. M., Brinkmann J., 2006, MNRAS, 368, 715
- Massey R., et al., 2007a, Nat, 445, 286
- Massey R., et al., 2007b, MNRAS, 376, 13
- Massey R., Refregier A., 2005, MNRAS, 363, 197
- Ngan W.-H. W., Van Waerbeke L., Mahdavi A., Heymans C., Hoekstra H., 2008, ArXiv e-prints: astro-ph/0809.3465
- Paulin-Henriksson S., Amara A., Voigt L., Refregier A., Bridle S. L., 2008, A&A, 484, 67
- Paulin-Henriksson S., Refregier A., Amara A., 2009, A&A, 500, 647
- Press W. H., Teukolsky S. A., Vetterling W. T., Flannery B. P., 1992, Numerical recipes in FORTRAN. The art of scientific computing. Cambridge: University Press, —c1992, 2nd ed.
- Refregier A., 2003, MNRAS, 338, 35
- Refregier A., Bacon D., 2003, MNRAS, 338, 48
- Rhodes J. D., Massey R. J., Albert J., Collins N., Ellis R. S., Heymans C., Gardner J. P., Kneib J.-P., Koekemoer A., Leauthaud A., Mellier Y., Refregier A., Taylor J. E., Van Waerbeke L., 2007, ApJS, 172, 203
- Sasiela R. J., 1994, Electromagnetic wave propagation in turbulence. Evaluation and application of Mellin transforms
- Schneider P., 2006, in Meylan G., Jetzer P., North P., Schneider P., Kochanek C. S., Wambsganss J., eds, Saas-Fee Advanced Course 33: Gravitational Lensing: Strong, Weak and Micro Part 3: Weak gravitational lensing. pp 269–451
- Schneider P., Kilbinger M., 2007, A&A, 462, 841
- Schneider P., Van Waerbeke L., Kilbinger M., Mellier Y., 2002, A&A, 396, 1
- Schneider P., Van Waerbeke L., Mellier Y., 2002, A&A, 389, 729
- Schrabback T., Erben T., Simon P., Miralles J.-M., Schneider P., Heymans C., Eifler T., Fosbury R. A. E., Freudling W., Hettetscheidt M., Hildebrandt H., Pirzkal N., 2007, A&A, 468, 823
- Schrabback T., et al., 2009, ArXiv e-prints: astro-ph/0911.0053
- Smith R. E., Peacock J. A., Jenkins A., White S. D. M., Frenk C. S., Pearce F. R., Thomas P. A., Efstathiou G., Couchman H. M. P., 2003, MNRAS, 341, 1311
- Spergel D. N., et al., 2007, ApJS, 170, 377
- Tian L., Hoekstra H., Zhao H., 2009, MNRAS, 393, 885
- Trotta R., 2008, Contemporary Physics, 49, 71
- Van Waerbeke L., Mellier Y., Hoekstra H., 2005, A&A, 429, 75